AGU100 ADVANCING EARTH AND SPACE SCIENCE

Timing and Pacing of Indonesian Throughflow Restriction and Its Connection to Late Pliocene Climate Shifts

Gerald Auer[1] iD, David De Vleeschouwer[2] iD, Rebecca A. Smith[3], Kara Bogus[4,5], Jeroen Groeneveld[2] iD, Patrick Grunert[6], Isla S. Castañeda[3], Benjamin Petrick[7], Beth Christensen[8], Craig Fulthorpe[9], Stephen J. Gallagher[10] iD, and Jorijntje Henderiks[11] iD

[1]Department of Biogeochemistry, Japan Agency for Marine-Earth Science and Technology, Kanagawa, Japan, [2]MARUM-Center for Marine and Environmental Sciences, University of Bremen, Bremen, Germany, [3]Department of Geosciences, University of Massachusetts Amherst, Amherst, MA, USA, [4]International Ocean Discovery Program, Texas A&M University, College Station, USA, [5]Camborne School of Mines, University of Exeter, Penryn, UK, [6]Institute of Geology and Mineralogy, University of Cologne, Cologne, Germany, [7]Max-Planck-Institut für Chemie, Mainz, Germany, [8]Environmental Studies Program, Adelphi University, Garden City, New York, USA, [9]Institute for Geophysics, University of Texas at Austin, Austin, TX, USA, [10]School of Earth Sciences, University of Melbourne, Melbourne, Victoria, Australia, [11]Department of Earth Sciences, Uppsala University, Uppsala, Sweden

Abstract The Pliocene was characterized by a gradual shift of global climate toward cooler and drier conditions. This shift fundamentally reorganized Earth's climate from the Miocene state toward conditions similar to the present. During the Pliocene, the progressive restriction of the Indonesian Throughflow (ITF) is suggested to have enhanced this shift toward stronger meridional thermal gradients. Reduced ITF, caused by the northward movement of Australia and uplift of Indonesia, impeded global thermohaline circulation, also contributing to late Pliocene Northern Hemisphere cooling via atmospheric and oceanographic teleconnections. Here we present an orbitally tuned high-resolution sediment geochemistry, calcareous nannofossil, and X-ray fluorescence record between 3.65 and 2.97 Ma from the northwest shelf of Australia within the Leeuwin Current. International Ocean Discovery Program Site U1463 provides a record of local surface water conditions and Australian climate in relation to changing ITF connectivity. Modern analogue-based interpretations of nannofossil assemblages indicate that ITF configuration culminated ~3.54 Ma. A decrease in warm, oligotrophic taxa such as *Umbilicosphaera sibogae*, with a shift from *Gephyrocapsa* sp. to *Reticulofenestra* sp., and an increase of mesotrophic taxa (e.g., *Umbilicosphaera jafari* and *Helicosphaera* spp.) suggest that tropical Pacific ITF sources were replaced by cooler, fresher, northern Pacific waters. This initial tectonic reorganization enhanced the Indian Oceans sensitivity to orbitally forced cooling in the southern high latitudes culminating in the M2 glacial event (~3.3 Ma). After 3.3 Ma the restructured ITF established the boundary conditions for the inception of the Sahul-Indian Ocean Bjerknes mechanism and increased the response to glacio-eustatic variability.

1. Introduction

The Indonesian Throughflow (ITF) is a key element of the global thermohaline circulation representing the last remaining tropical connection facilitating warm water exchange between the world's oceans (Kuhnt et al., 2004; Gallagher et al., 2017; Figure 1 and see supporting information text S1 for details on the physical oceangraphic setting). Modeling studies suggest that ITF variability has a major influence on ocean heat distribution (Brierley & Fedorov, 2011; Cane & Molnar, 2001; Di Nezio et al., 2016; Jochum et al., 2009), yet its contribution to the global climatic evolution is difficult to resolve due to the tectonic complexity of the Indonesian Archipelago (Brierley & Fedorov, 2011; Gordon et al., 2010; Gordon & Kamenkovich, 2010; Holbourn et al., 2011; Kuhnt et al., 2004; Spooner et al., 2011; Susanto & Song, 2015). Generally, ITF restriction is likely driven by two distinct mechanisms: (1) sea level-driven restriction leading to the emergence of shelf areas restricting the ITF paths only to the deep marine troughs during glacial intervals (De Vleeschouwer et al., 2018; Di Nezio et al., 2016; Holbourn et al., 2011; Xu et al., 2008, 2006; Zuraida et al., 2009); and (2) geometric reorganization of the Indonesian Gateway system caused by tectonic activity linked to the northward movement of the Australasian Plate and the related collision with the Eurasian Plate (Cane
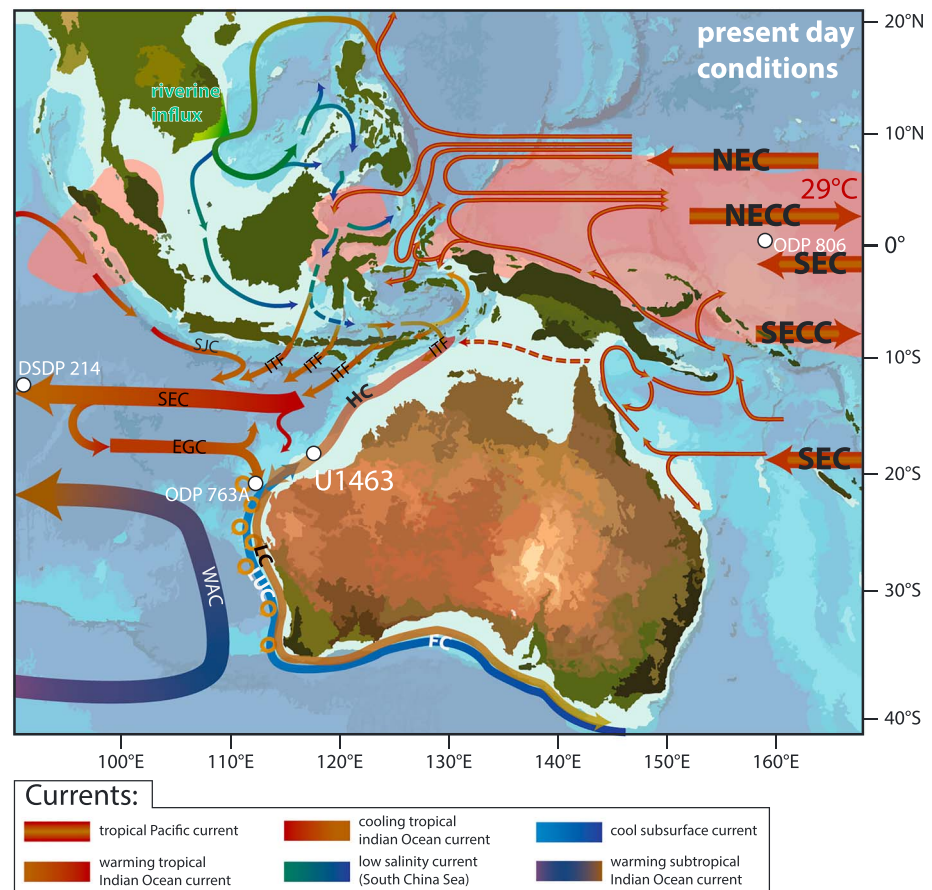
Figure 1. Map showing the position of Sites U1463, Ocean Drilling Program (ODP) 763A, ODP 806, and Deep See Drilling Project (DSDP) 214 (white dots) in relation to the major current paths of the Indonesian Throughflow (ITF) and the eastern Indian Ocean. Color gradients denote temperature (red-blue) and salinity (green) gradients within the currents. Current paths along Western Australia were adapted from Furue et al. (2017), Wijeratne et al. (2018), and B. Wilson (2013)). The dominant throughflow paths and major equatorial Pacific and Indonesian currents are based on observations and models in Gordon et al. (2010) and Schiller et al. (2007, 2010). Green arrows indicate monsoonal freshwater discharge into the South China Sea from major Southeast Asian rivers (i.e., Mekong-, Pearl-, and Red River). Red shaded ocean areas represent the outer boundary of the 29 °C isotherm of the Indo-Pacific Warm Pool. Colors on land approximate current vegetation cover in Australia and the maritime continent from satellite images. Base map and satellite images used to generate this figure were generated in GeoMapApp (http://www.geomapapp.org). Pacific currents: North Equatorial Current (NEC), North Equatorial Counter Current (NECC), South Equatorial Current (SEC), and South Equatorial Counter Current (SECC). Indian Ocean currents: Indonesian Throughflow (ITF = dominant outflows from the Indonesian Archipelago), South Java Current (SJC), South Equatorial Current (SEC), East Gyral Current (EGC), Holloway Current (D'Adamo et al., 2009; B. Wilson, 2013), and Leeuwin Current (LC), which are considered as one current system in this work, Leeuwin Undercurrent (LUC), West Australia Current (Schott et al., 2009).

& Molnar, 2001; Christensen et al., 2017; Karas et al., 2017; Kuhnt et al., 2004; Molnar & Cronin, 2015; Sarnthein et al., 2017).

There is evidence suggesting that an important uplift phase began during the Late Miocene to Early Pliocene (Cane & Molnar, 2001; Hall, 2002; Hall et al., 2011; Kuhnt et al., 2004; Molnar & Cronin, 2015; Tate et al., 2017), with tectonic restriction of the ITF having a major effect on global thermohaline circulation by the late Early Pliocene (Cane & Molnar, 2001; Gallagher et al., 2009; Karas et al., 2009, 2011b; Karas et al., 2017). The ITF reorganization during the Pliocene has also been causally linked to the marine isotope stage (MIS) M2 glacial event at ~3.3 Ma (Brigham-Grette et al., 2013; De Schepper et al., 2014, 2013; Lisiecki & Raymo, 2005) with modeling and paleoceanographical studies showing that tectonic ITF restriction had major effects on global climate by changing the heat exchange between the Pacific and the Indian Oceans (Cane & Molnar, 2001; De Schepper et al., 2014; De Vleeschouwer et al., 2018; Gallagher et al., 2009;

Gallagher et al., 2017; Karas et al., 2009, 2011b; Karas et al., 2017; Molnar & Cronin, 2015; Sarnthein et al., 2017). The MIS M2 event is of particular interest as it represents a well-recognized feature of global benthic oxygen isotope records of both the LR04 stack (Lisiecki & Raymo, 2005) and DV17 mega splice (De Vleeschouwer et al., 2017). The M2 event was also interpreted as a failed attempt of the Earth's climate state to shift to Pleistocene-like glacial-interglacial mode (e.g., Haug & Tiedemann, 1998). More recently, a link between Australian climate and Pliocene ITF restriction in relation to the changing Australian monsoon system was postulated by Christensen et al. (2017). Sarnthein et al. (2017) further proposed possible teleconnections linking changes in ITF to Mediterranean Outflow variability in the Pliocene through a complex interhemispheric coupled ocean/atmospheric teleconnection via the Indian Ocean and Africa. This is controlled by the so called "Sahul-Indian Ocean Bjerknes Mechanism," linked to sea level-driven changes in landmass configuration (Di Nezio et al., 2016). The "Sahul-Indian Ocean Bjerknes Mechanism" proposed by Di Nezio et al. (2016) amplifies changes in Indian Ocean atmospheric circulation by increasing east-west sea surface temperature (SST) gradients similar to the Bjerknes mechanism in the Pacific (Bjerknes, 1969). The mechanism leads to a positive feedback with ocean dynamical processes amplifying externally forced climatic changes in the Indian Ocean during glacial sea level lowstands (Di Nezio et al., 2016).

In this study we present a multiproxy data set spanning the Early to Late Pliocene (~3.66 to 2.98 Ma) from International Ocean Discovery Program (IODP) Expedition 356 Site U1463 (Gallagher et al., 2017), situated on the Australian northwest shelf (NWS) within the path of the Leeuwin Current (LC), and directly influenced by the ITF (D'Adamo et al., 2009; Wijeratne et al., 2018). The high recovery of material at Site U1463 (Christensen et al., 2017; De Vleeschouwer et al., 2018; Gallagher et al., 2017) permits the reconstruction of high-resolution record of Pliocene downstream ITF variability along the NWS. Geophysical borehole records and sedimentological data from Expedition 356 have already proven instrumental in detailing the long-term climatic evolution of Australia throughout the Neogene (Christensen et al., 2017; Groeneveld et al., 2017). Here we elucidate surface water conditions along the NWS in the critical Pliocene time interval between 3.5 and 3 Ma, when tectonic ITF restriction is proposed to have significantly altered the ITF (Cane & Molnar, 2001; Christensen et al., 2017; De Vleeschouwer et al., 2018; Gourlan et al., 2008; Karas et al., 2009; Le Houedec et al., 2012). We applied an integrated approach using paleobiological (calcareous nannofossil assemblages), geochemical (planktic foraminifer stable isotopes and bulk organic carbon, sulfur, and carbonate content), and geophysical data including calibrated spectral gamma ray and X-ray fluorescence (XRF) elemental data (De Vleeschouwer et al., 2018) to reconstruct environmental changes along the NWS and link them to contemporary climatic records in the region (Karas et al., 2009, 2011b; Wara et al., 2005).

Our study provides novel insights into the temporal evolution of Pliocene ITF restriction in relation to global climatic changes and investigates how tectonic ITF restriction and the transport of tropical waters from the Pacific into the Indian Ocean may have increased the sensitivity of the Indian Ocean to orbitally driven Antarctic ice sheet dynamics (Patterson et al., 2014), which potentially amplified the cooling during the MIS M2 glacial event at 3.3 Ma in the Southern Hemisphere (De Vleeschouwer et al., 2018). To achieve this, we present a detailed timeline of how changes in ITF configuration heralded major changes in the eastern Indian Ocean, which in turn affected global climatic patterns (Christensen et al., 2017; De Schepper et al., 2014; Gallagher et al., 2009; Karas et al., 2009, 2011b; Karas et al., 2017; Sarnthein et al., 2017). We also provide the first evidence for the increasingly important role glacio-eustatic sea level changes had on the Indian Ocean hydroclimate after MIS M2 and show how they are linked to the shift in the Australian climate system from a "humid interval (5.5–3.3 Ma)" to a "transitional interval (3.3–2.4 Ma)" (Figure 2 in Christensen et al., 2017).

2. Materials and Methods

Site U1463 (145-m water depth; 18°59′S, 117°37′E; Figure 1) yielded an expanded Plio-/Pleistocene record directly within the path of the LC downstream of the ITF (Figure 1; D'Adamo et al., 2009; De Deckker, 2016; Gallagher et al., 2017; Wijeratne et al., 2018). Its sediments represent outer shelf to shallow bathyal (~400- to 1,200-m water depth; Gallagher et al., 2017) mixed carbonate and siliciclastic fine-grained sediments rich in planktic and benthic foraminifers as well as calcareous nannofossils. The material represents a continuous paleoecological record of the Pliocene.

Cores were sampled from Holes U1463B, U1463C, and U1463D between 277.84-m core composite depth below sea floor (CCSF) and 312.84 m CCSF with a continuous resolution of 20 cm. The targeted interval was anchored between the last occurrence of *Reticulofenestra pseudoumbilicus* (>7 μm; 3.7 Ma) and the last occurrence of *Discoaster tamalis* (2.8 Ma; Figure S1 and Table S1). For all subsequent analyses, we used the revised splice of De Vleeschouwer et al. (2018), which refines the shipboard splice that was generated on board to a depth of 275.88 m below sea floor (Gallagher et al., 2017). The age model used for this study was refined by tuning the $\delta^{18}O_{T.\ sacculifer}$ record published in De Vleeschouwer et al. (2018) to austral eccentricity-tilt-precession (ETP) composite derived from the LA04 (Laskar et al., 2004) astronomical solution, with the differences between the age models shown in Figure S2. The discrepancy between the current age model age-depth model and the age-depth model of De Vleeschouwer et al. (2018) never exceeds 0.04 Ma. The refined age model results in an average sample resolution of ~4 kyr that allowed for independent correlation with other Indian Ocean and IPWP Sites.

2.1. Calcareous Nannoplankton

A total of 172 samples (Table S2) were prepared for calcareous nannoplankton assemblage studies and biostratigraphy following the methods of Bordiga et al. (2015). Five milligrams of freeze-dried sample were suspended in 50 ml of NH_3 buffered ultrapure milli-Q water. The suspension was ultrasonicated for ~30 s and subsequently 1 to 1.5 ml were transferred onto a 30×24 mm cover slip. Buffered milli-Q water was added to reach a total volume of 1.5 ml on the cover slip, sufficient to fully cover its entire surface area. After slowly drying on a hot plate (~50 °C) the cover slip was mounted on a standard microscopy slide using Norland No. 61® optical mounting medium and cured under ultraviolet light. Slides were examined using standard polarized light microscopy (Olympus BX53, Japan Agency for Marine-Earth Science and Technology, JAMSTEC) and scanning electron microscopy imaging (Zeiss Gemini DSM 982, University of Graz). For assemblage work at least two transects consisting of 24 field views with 1-mm spacing were counted along the short axis within the first and third quarter of the cover slip. Additional transects were counted if the minimum number of specimens was not reached. Absolute number of identifications per slide is consequently dependent on overall nannoplankton abundance in each sample. On average ~600 specimens were identified per sample (Table S2). Table S2 also contains total nannofossil abundances as coccoliths per gram of sediment ($N/g_{sediment}$; cf. Bordiga et al., 2015).

2.1.1. Taxonomic Remarks

Taxonomic identification is based on Perch-Nielsen (Perch-Nielsen, 1985) and Young (Young, 1998) and supplemented by the Handbook of Calcareous Nannoplankton 1–5 (Aubry, 1984, 1988, 1989, 1990, 1999) and the Nannotax3 website (Young et al., 2014), with additional taxonomic notes given in the supporting information Text S2. The taxonomic distinction of the reticulofenestrids (genus *Reticulofenestra* and *Gephyrocapsa*; Figures 2a, 2b, and 2e, and S3) is poorly defined in the Neogene (see Young, 1998, for discussion). *Reticulofenestra* species are generally distinguished by placolith size, with various research groups using different size ranges (Gibbs et al., 2005; Imai et al., 2017; Jatiningrum & Sato, 2017; Wade & Bown, 2006). In this study we distinguished different species of the reticulofenestrids using the following taxonomic criteria:

|	
Small *Gephyrocapsa* sp.:	reticulofenestrids <3 μm in length with a distinct angled bar spanning the central area.
Medium *Gephyrocapsa sp.*:	reticulofenestrids >3 μm in length with a distinct angled bar spanning the central area (maximum recorded length of specimens of this morphotype is 3.8 μm in the studied samples).
Reticulofenestra minuta:	reticulofenestrids <3 μm in length without a bar spanning the central area.
Reticulofenestra haqii:	reticulofenestrids 3–5 μm in length with an open central area.
Reticulofenestra antarctica:	reticulofenestrids 3–5 μm in length with a closed central area.
Reticulofenestra pseudoumbilicus (small):	all reticulofenestrids 5–7 μm in length.
Reticulofenestra pseudoumbilicus (sensu stricto):	all reticulofenestrids >7 μm in length.
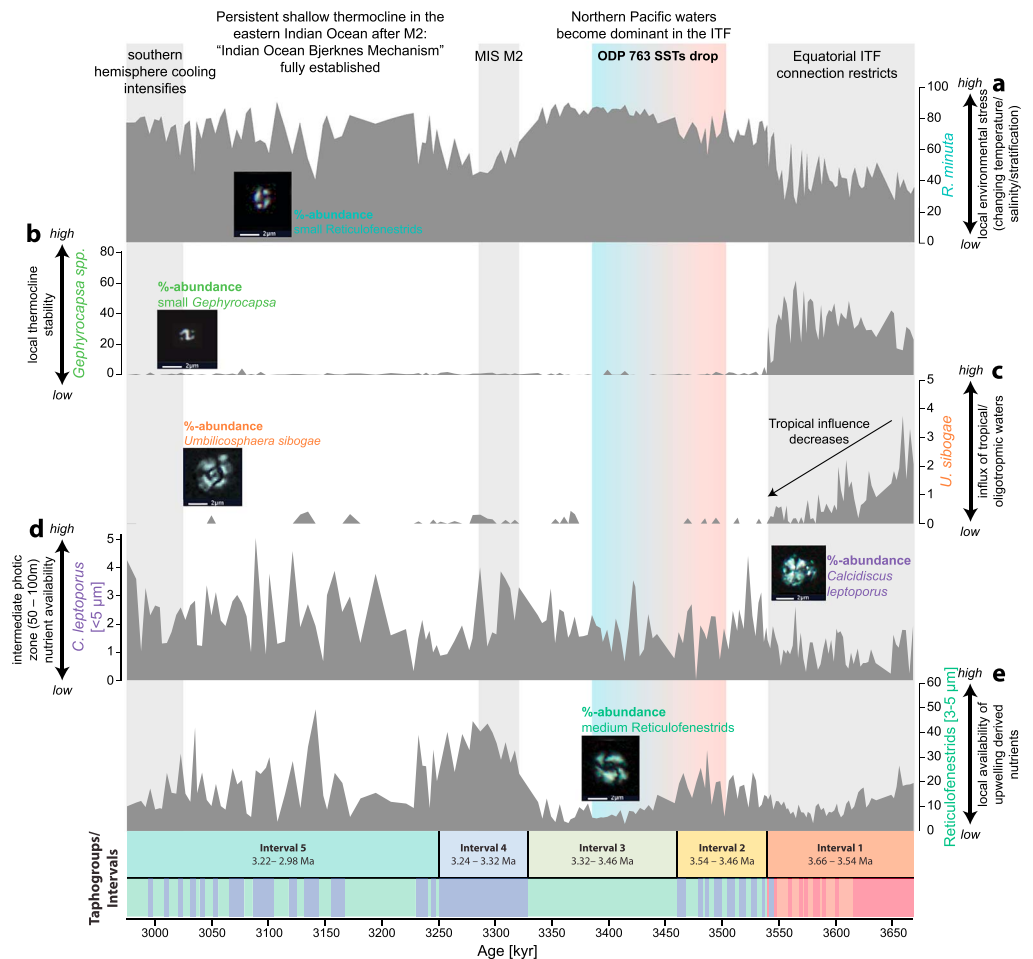
Figure 2. Geochemical and calcareous nannofossil and data converted to age (in kyr) based on the refined age model of De Vleeschouwer et al., 2018 and plotted together with the intervals defined by cluster analysis (see Figure S3 for comparison). Underlay represents major events at the northwest shelf . Gray bars are showing proposed Indonesian Throughflow (ITF) restriction ~3.54 Ma, extend of marine isotope stage M2 ~3.31–3.26 Ma (Lisiecki & Raymo, 2005); the proposed intensification of Southern Hemisphere cooling (Riesselman & Dunbar, 2013) and/or northern hemisphere cooling beginning to affect the tropics (Philander & Fedorov, 2003) ~3.0 Ma. Cooling at Site 763A between 3.5 and 3.4 Ma (Karas et al., 2011b) is shown as a colored (red-blue) interval. These intervals are used to anchor long-term trends (= text at top of the figure) in the data shown: (a) abundance of *Reticulofenestra minuta* indicating stressed environmental conditions; (b) abundance of small *Gephyrocapsa*, with the end of its acme at Site U1463 clearly visible ~3.54 Ma; (c) abundance of *Umbilicosphaera sibogae* (note the decrease toward 3.54 Ma); (d) abundance of *Calcidiscus leptoporus* susp. small, note the pulses in abundance after 3.54, 3.35, and 3.20 Ma, and the high variability after 3.20 Ma; (e) abundance of medium sized reticulofenestrids (combining *Reticulofenestra haqii* and *R. antarctica*). Note the three distinct pulses in abundance ~3.54, ~3.35, and ~3.20 Ma.

2.1.2. Statistical Analyses

Total calcareous nannofossil abundance was converted to relative abundance, to avoid effects from changes in sedimentation rates on nannofossil accumulation over the studied interval. For diversity analysis several indices were calculated including the total taxa present (Table S2), species evenness (J'; Figure S3m and Table S2), and the classical Shannon-Wiener diversity index (H'; Figure S3n and Table S2; Auer et al., 2014; Sokal & Rohlf, 1995). To avoid issues arising from potentially nonnormal multivariate distribution, the relative nannofossil abundances were arcsine root transformed (e.g., Sokal & Rohlf, 1995) prior to cluster analysis (Figures S4 and S5) and principal component analysis (PCA; Figure S6), as incorporated in the statistics package PAST (v3.16; Hammer et al., 2001). Hierarchical clustering in this study used Ward's method (e.g., Sokal & Rohlf, 1995) with Euclidean similarity (Hammer & Harper, 2006; Sokal & Rohlf, 1995; Ward, 1963), to group samples with similar assemblage composition. Major clusters were defined using a cutoff

similarity of <0.75. Subclusters were defined based on visual separation of the clusters at different similarity values in each major cluster. Following cluster definition for the sample set, PCA using the Bray-Curtis similarity was performed (Hammer & Harper, 2006; Sokal & Rohlf, 1995), which shows the sample distribution in the two-dimensional space expressed by principle components PC1 and PC2, defining the orthogonal space that accounts for the highest variance in the sample set (Hammer & Harper, 2006; Sokal & Rohlf, 1995). To test the validity of the results, bootstrapping ($N = 1,000$) was applied. Furthermore, a second analysis was run using the unweighted pair group method with arithmetic mean (UPGMA) hierarchical clustering with Bray Curtis similarity (Bray & Curtis, 1957; Hammer & Harper, 2006; Sokal & Rohlf, 1995; bootstrap $N = 1,000$; Figure S5). For the final interpretation we relied on Ward's method since it was designed to create well defined clusters, which were supported by the results of UPGMA clustering (Figures S4 and S5). To explore the contribution of individual taxa to the clusters, a similarity percentage analysis (SIMPER; Sokal & Rohlf, 1995) was performed using Bray-Curtis similarity. Subsequently, intervals with similar cluster distribution were grouped together, to show larger trends and shifts in assemblage composition. The defined intervals where then evaluated with regard to the distribution of individual nannofossil taxa within them and reflect mean paleoenvironmental conditions that persisted at Site U1463 using available information on the ecological preferences of the present nannofossil taxa. Cluster analysis was also run excluding nannofossil taxa with global extinctions events during the study interval (i.e., *Sphenolitus* spp.) to test the contribution of its extinction to the cluster distribution. As exclusion did not affect cluster distribution significantly, the taxon was included in the statistical analysis as patterns of decline preceding extinction events can still provide valuable information on local paleoenvironmental changes (Gibbs et al., 2004, 2005).

2.2. Carbon and Sulfur Analysis, and Calcite Equivalent Carbonate Content

Total carbon (TC) and sulfur content was determined for 207 samples on and off the splice (Table S3). For analysis ~0.1 g of freeze-dried and ground sample were measured using a Leco CS-300 carbon and sulfur analyzer (University of Graz). For total organic carbon (TOC) analysis ~0.1 g of freeze-dried and ground sample was fully decalcified using stepwise addition of 2N HCl. After decalcification samples were washed with distilled water to remove excess HCl and dried before being measured. Calcite-equivalent carbonate content $CaCO_{3(calcite-eq.)}$ (Table S3) was calculated by using the stoichiometric formula: $CaCO_{3(calcite-eq.)} = (TC - TOC) \times 8.34$ (Grunert et al., 2010; Stax & Stein, 1995). For brevity $CaCO_{3(calcite-eq.)}$ is referred to as $CaCO_3$ or "carbonate content" hereafter. The C/S ratio was calculated using TOC and sulfur concentrations (Table S3).

2.3. XRF Elemental Analysis

The relative elemental composition of Site U1463 sediment cores was determined by measuring split core surfaces with a third generation Avaatech XRF core scanner at the XRF Core Scanning Facility of the Gulf Coast Repository at Texas A&M University (De Vleeschouwer et al., 2018). Measurements were taken every 2 cm at source energies of 9 kV (no filter) and 30 kV (Pd filter, 1.25 mA). Idle time for each measurement was 6 s. Element intensities were obtained by converting the raw XRF spectra using the iterative least squares software package from Canberra Eurisys (WIN AXIL). Due to drilling disturbance, several core sections were not scanned and consequently appear as gaps in the record (Figure 3e); XRF core scanning results are reported as natural logarithmic ratios. We used elemental ratios to infer relative changes in total terrigenous influx, defined as $\ln((Al + K)/Ca)$, as well as dust flux (i.e., the flux of heavy minerals such as zircon and rutile), defined as $\ln((Fe + Ti + Zr)/(Al + K))$, at Site U1463. These ratios and their use as paleoclimate proxies are similar to those from Holocene sediment cores from the Timor Sea, north of Site U1463 (Kuhnt et al., 2015). However, we included Al in our proxy for total riverine influx, to account for potential changes in weathering rates on the Australian continent, which may change the ratio of illite/smectite to kaolinite (Ehrmann et al., 2013; Gingele et al., 2001; Gingele & De Deckker, 2004; Wei et al., 2006). The $\ln((Al + K)/Ca)$ ratio was subsequently compared to discrete measurements of carbonate content (Figure 3e).

2.4. Recalculated Mg/Ca Temperatures and Ice Volume Corrected $\delta^{18}O$ Values of Sea Surface Water

Trilobatus sacculifer Mg/Ca temperature records from Ocean Drilling Program (ODP) Site 806 (Wara et al., 2005; red graph in Figure 4a) and Site 763 (Karas et al., 2011b; blue graph in Figures 3a and 4a) were
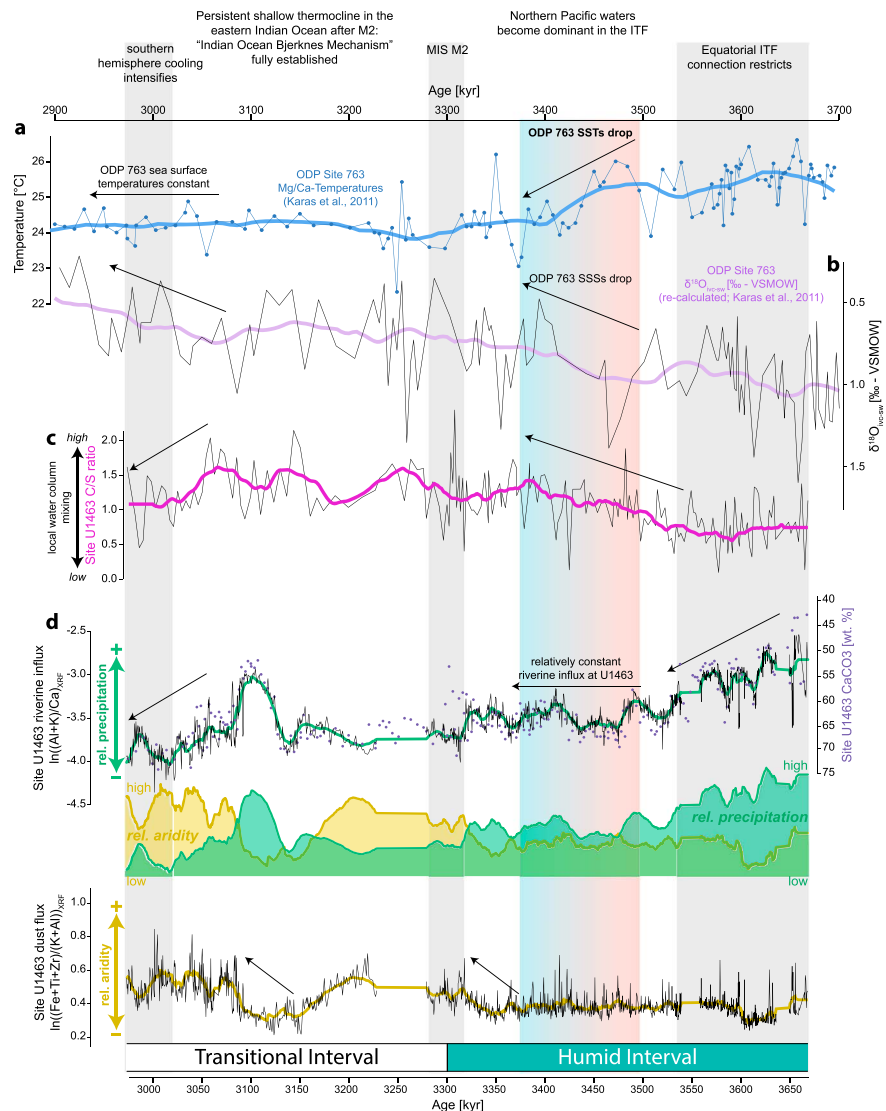
Figure 3. Comparison of long-term oceanographic trends between 3.56 and 2.97 Ma along the northwest shelf at sites 763A (Karas et al., 2011b) and Site U1463 with climatic conditions in the Australian hinterland (Christensen et al., 2017; De Vleeschouwer et al., 2018; this study), major events as defined in Figure 3 are again shown: (a) Site 763A Ca/Mg temperature record (Karas et al., 2011b), showing SSTs decreasing south of Site U1463 shortly after the assemblage shift ~3.54 Ma (black arrow); (b) recalculated $\delta^{18}O_{ivc-sw}$ (Karas et al., 2011b) showing two intervals of increased sea surface water freshening (black arrows) at Site 763A; (c) C/S ratio showing bottom water oxygenation as a proxy for water column mixing at Site U1463. (d) X-ray fluorescence (XRF) elemental ratios $\ln((K + Al)/(Ca))$ (= riverine influx) and $\ln((Fe + Ti + Zr)/(Al + K))$ (= dust flux) are shown with their long-term trends (21 pt. running mean). Discrete measurements of calcite equivalent calcium carbonate content (wt.%; blue dots) are shown in conjunction with the $\ln((K + Al)/(Ca))$ record. The running means of the XRF records were superimposed to show relative changes in precipitation (riverine influx) versus aridity (windblown dust) at Site U1463. This long-term comparison uses the same scale as their respective XRF ratios plotted below and above. Below the XRF records the transition between humid and transitional intervals (after Christensen et al., 2017) at 3.3 Ma is shown. MIS = marine isotope stage; ITF = Indonesian Throughflow.

recalculated to compare them to each other using the species specific equation (Mg/Ca = 0.377×exp(0.09×T)) given in Anand et al. (2003). Deep See Drilling Project (DSDP) Site 214 sea surface temperatures are based on a combined record of *T. sacculifer* (light gray dots) and *Globigerinoides ruber* (black dots) published by Karas et al. (2009; orange graph in Figure 4a). *G. ruber* Mg/Ca temperature records were calculated using the species specific equation (Mg/Ca = 0.395×exp(0.09×T); Anand et al., 2003). DSDP
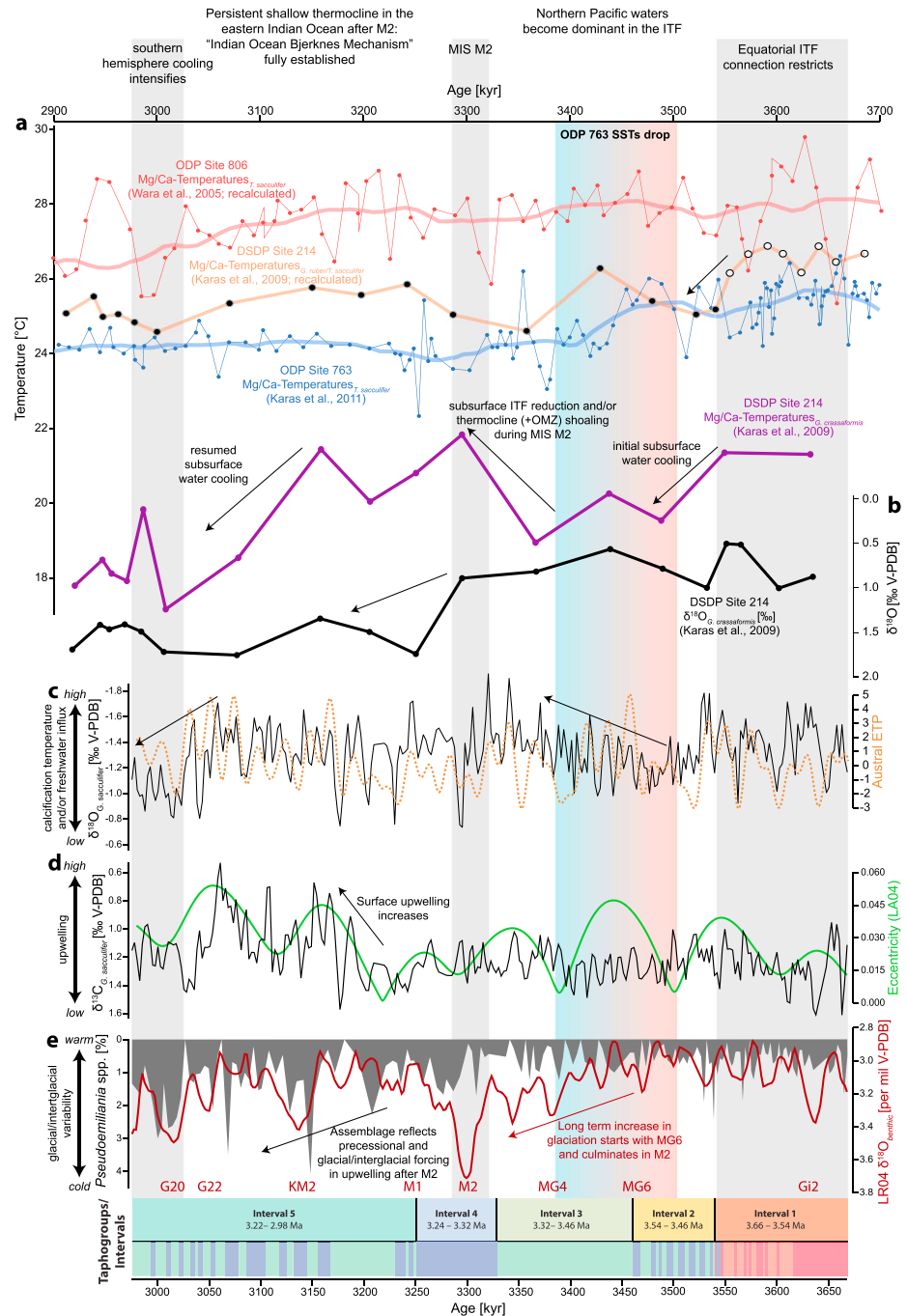
Figure 4. Temperature records (Deep See Drilling Project [DSDP] Site 214 and Ocean Drilling Program [ODP] sites 763A and 806) in comparison with selected data from Site U1463 (De Vleeschouwer et al., 2018; this study) to illustrate the relative progression of events in Pliocene ITF restriction (see Figure 2) between 3.56 and 2.97 Ma in the larger context of the tropical Indo-Pacific region (Figure 1). (a) Comparison of surface Mg/Ca temperature records from DSDP Site 214 (orange) and ODP Sites 763A (blue; 11-pt running mean) and 806 (red; 11-pt running mean), as well as the subsurface *G. crassaformis* record from Site 214 (purple). All temperature records are plotted on the same temperature scale; (b) Site 214 subsurface $\delta^{18}O_{G.\ crassaformis}$ data (Karas et al., 2009). (c) $\delta^{18}O_{T.\ sacculifer}$ (De Vleeschouwer et al., 2018) shown together with austral ETP calculated from the LA04 astronomical solution (Laskar et al., 2004); note long-term shifts between 3.54 and 3.40 Ma as well as after 3.05 Ma. (d) Site U1463 $\delta^{13}C_{T.\ sacculifer}$ data showing a significant drop related to increased upwelling along the northwest shelf after marine isotope stage (MIS) M2, record is shown together with the eccentricity curve from the LA04 astronomical solution (Laskar et al., 2004). (e) LR04 benthic isotope stack (Lisiecki & Raymo, 2005) superimposed on the abundance of *Pseudoemiliania* spp. showing the increasing respond to glacial/inter-glacial cyclicities after MIS M2. ITF = Indonesian Throughflow.

Site 214 subsurface temperatures are derived from *Globorotalia crassaformis* (Karas et al., 2009) and calculated using the equation Mg/Ca = 0.339×exp(0.09×*T*) (purple graph in Figure 4a; Anand et al., 2003).

To calculate the temperature-corrected oxygen, isotope values of surface waters ($\delta^{18}O_{sw}$) the equation of Bemis et al. (1998) and Thunell et al. (1999) expressed as

$$\delta^{18}O_{sw}(V\text{–SMOW}) = 0.27 + \frac{T(^{\circ}C) - 16.5 + 4.8*\delta^{18}O_{calcite}(V\text{–PDB})}{4.8}$$

was applied to the Site 763A $\delta^{18}O_{T.\ sacculifer}$ data of Karas et al., 2011b; Figure 3a). To correct for the $\delta^{18}O$ offset of changing ice volume ($\delta^{18}O_{icv\text{-}sw}$), we followed the same approach as Karas et al. (2011a). The benthic $\delta^{18}O$ of the LR04 isotope stack (Lisiecki & Raymo, 2005) was normalized to the modern value and reduced to 75%, to account for the ~0.87–1.3‰ last glacial/interglacial global ice volume difference before subtracting it from the calculated $\delta^{18}O_{sw}$ values (Karas et al., 2011a; Schrag et al., 2002; Waelbroeck et al., 2002).

3. Results

3.1. Calcareous Nannofossil Assemblages

3.1.1. Preservation

Generally, nannofossil preservation is moderate to moderately good in the sampled interval (Gallagher et al., 2017). Under both scanning electron microscopy and light microscopy, frequent overgrowth was observed especially on specimen of *Calcidiscus* spp.; reticulofenestrids were largely unaffected by noticeable overgrowth. Calcareous nannofossil preservation was inversely correlated to carbonate content resulting in the best preservation occurring in the lowermost section. Total nannofossil abundances ($N/g_{sediment}$) shows a low correlation with species evenness ($r = -0.122$; Figure S3 and Table S2), indicating that low diversity is not an effect of low abundance (i.e., selective dissolution of more fragile taxa).

3.1.2. Nannofossil Diversity

Nannofossil diversity was generally moderate to low, which is typical for shelf environments. A total of 34 taxa were identified with median diversity of 13 taxa per sample (maximum = 21, minimum = 6; Table S2). Both species evenness and Shannon diversity index show a strong trend through time (Figure S3). Species evenness progressively decreases from the base of the record (~3.65 Ma) until reaching a minimum at ~3.4 Ma. After 3.4 Ma species evenness increases again, reaching a new steady state by 3.3 Ma and displaying strong variability until the end of the studied interval (~2.98 Ma). The Shannon diversity index similarly decreases between ~3.66 and 3.41 Ma before showing a marked diversity increase from ~3.31 to 3.23 Ma exhibiting strong short-term variability until 2.97 Ma.

3.1.3. Cluster and SIMPER Analysis

Cluster analysis (Ward's method) resulted in three clusters representing sample groups with a similar nannofossil assemblage composition. The clusters were defined at a cutoff distance of ~2.5 with a cophenetic correlation coefficient of 0.90. Bootstrapping provided good support for the separation between all three clusters (Figure S4). Separation between the three defined clusters was also strongly supported by bootstrapped results of the UPGMA clustering using Bray-Curtis similarity (cophenetic correlation: 0.89; Figure S6). Ward's method bootstrapping also supported the separation of cluster 1 into two subclusters with a relatively low distance of ~1.5; however, this was not supported by UPGMA. While we show the two subclusters in Figures 2, 4, and S3 and also cluster dendrograms and PCA (Figures S4–S6) for methodological veracity, we did not consider them in subsequent data treatment and interpretation. This decision is based on their low distance and weak support in UPGMA, which suggests that the two subclusters may not reflect an unambiguous paleoecological signal. The exclusion of *Sphenolithus* spp. from cluster analysis was also tested and showed no significant changes in clustering, indicating that local paleoenvironmental conditions are the main factor controlling cluster distribution. SIMPER analysis (Table S4) using Bray Curtis similarity showed that the separation of the three main clusters can be mainly explained by the abundance of *R. minuta*, *R. haqii* and *R. antarctica*, as well as the presence of *Gephyrocapsa* spp., *U sibogae* and *Sphenolithus* sp. These had contributions >3% and cumulatively accounted for ~71.7% of the total variance between the defined clusters (Table S5). The clusters are thus representative of similar nannofossil taphocoenoses present in each sample, which can be summarized as taphogroups (e.g., Auer et al., 2014):

Taphogroup (TG)1 consists of two subgroups defined by cluster 1A and 1B and dominates the base of the studied interval from 312.84 to 302.14 m CCSF (~3.65–3.50 Ma). TG1 is defined by the high abundances of small *Gephyrocapsa* (average ~36.2%), *Reticulofenestra minuta* (~41.2%), *R. haqii* (~8.6%), and *Sphenolithus* spp. (~4.8%). The occurrence of *Umbilicosphaera sibogae* (up to ~3%) within this TG was notable; *TG2* is formed by cluster 2 and reflects taphocoenoses still dominated by *R. minuta* (average ~61.4%) with a high contribution of *R. antarctica* (~13%) and *R. haqii* (~16.2%). TG2 exhibits the highest average contribution of *C. leptoporus* subsp. small (~2.1%) and is the only TG with a contribution of *Pseudoemiliania* sp. above 1% (average ~1.1%). *TG3* is formed by cluster 3 and reflects taphocoenoses dominated by *R. minuta* (average ~82.5%) with subordinate contributions of *R. haqii* (~7.2%). Notable is the low abundance of *R. antarctica* (~3.3%) and the similar but slightly lower *Calcidiscus leptoporus* subsp. small (~2%) compared to TG2. Numerical differences in taxon abundance of the defined TGs are summarized in Table S5.

3.2. Geochemical proxies

3.2.1. XRF-Based Proxies for Riverine Input and Dust Flux

We used $\ln((Al + K)/Ca)$ as a proxy for riverine input since Site U1463 is likely to contain terrigenous material from both direct riverine influx as well as windblown particles from arid regions. Furthermore, despite its higher water depth (~400–1,200 m) in the Pliocene (Gallagher et al., 2017), the sites setting on the NWS may result in significant contributions of both benthic and planktic carbonates. We thus compared the $\ln((Al + K)/Ca)$ ratio to both discrete measurements of $CaCO_3$ and to total nannofossil abundances ($N/g_{sediment}$). The high inverse correlation of carbonate content with $\ln((Al + K)/Ca)$ ($r = -0.82$; Figures 3e and S7a) and low correlation with total nannofossil abundances ($r = -0.33$, Figure S7b) indicates that $\ln((Al + K)/Ca)$ is controlled by $CaCO_3$ content but planktic carbonate production does not control total carbonate content at Site U1463 over the studied interval. Total nannofossil abundances are also weakly correlated to $\ln((Al + K)/Ca)$ ($r = 0.46$, Figure S7c). As $CaCO_3$ is lowest when sedimentation rates are high (Figure S7d), it can be assumed that carbonate content is predominantly forced by riverine influx and not the deposition of carbonate producers (both benthic and planktic) on the NWS during the Pliocene. The $\ln((Al + K)/Ca)$ ratio is also highly correlated with NGR derived and XRF derived potassium concentrations ($r = 0.98$, not plotted) used in previous studies to characterize riverine influx at Site U1463 (Christensen et al., 2017; De Vleeschouwer et al., 2018).

The use of $\ln((Fe + Ti + Zr)/(Al + K))$ as a dust proxy is supported by its negative correlation ($r = -0.69$) to $\ln((Al + K)/Ca)$ thereby showing an inverse relationship of dust flux compared to riverine sources of terrigenous material (Figure 3e). The two ratios together thus reflect relative changes between humidity and aridity on the Australian hinterland at Site U1463 (Figure 3e). The $\ln((Al + K)/Ca)$ ratio shows a progressive decrease between 3.66 and 3.45 Ma reflecting declining riverine influx at Site U1463 (Figure 3e). After 3.30 Ma terrigenous influx stays relatively low apart from a short (~80 kyr) increase from 3.15 to 3.10 Ma, which represents a disruption in the long-term progressive reduction of riverine input that continues until ~2.97 Ma. Dust flux at Site U1463 remains stable and relatively low before increasing around 3.33 Ma, at the end of the Australian Humid Interval of Christensen et al. (2017; Figure 4e). Subsequently, dust flux reduces simultaneously with increasing riverine influx between 3.15 and 3.10 Ma. Dust flux then increases again until ~3.00 Ma and remains high until the end of the studied interval at 2.97 Ma.

3.2.2. C/S Ratio

The C/S ratio reflecting changes between organic carbon burial and sulfate reduction shows relatively low values between 3.66 and 3.55 Ma before increasing and reaching a new steady state by 3.39 Ma (Figure 3c). This state of relatively high but variably values persists until a further short increase between 3.16 and 3.04 terminates the interval of increased C/S values by again dropping significantly around 3.04 until 2.97 Ma.

4. Discussion

4.1. Calcareous Nannofossil Paleoecology

While the exact ecological parameters for individual calcareous nannoplankton taxa are often difficult to pinpoint even in the modern ocean (e.g., Baumann et al., 2005; Boeckel et al., 2006; Boeckel & Baumann, 2004, 2008; Bollmann, 1997; Cachão et al., 2000; Okada & Honjo, 1973; Silva et al., 2008; Ziveri et al., 2004), it is still possible to make generalized inferences on their ecological preferences in the past (e.g.,

Auer et al., 2014, 2015; Ballegeer et al., 2012; Couapel et al., 2007; De Schepper et al., 2011; Gibbs et al., 2004; Grelaud et al., 2009; Lees et al., 2005; Marino et al., 2014; Saavedra-Pellitero et al., 2014; Wade & Bown, 2006). Changes in nannofossil assemblage composition in the absence of significant dissolution or reworking are thus reflective of changing paleoenvironmental conditions over time. The three taphogroups defined by cluster analysis can be interpreted to represent distinct paleoenvironmental conditions at Site U1463.

Taphogroup 1 (TG1) represents a warm to tropical neritic assemblage with high abundance of small *Gephyrocapsa* sp. (Figures 2b and S3c) and *Reticulofenestra minuta* (Figures 2a and S3g). Comparatively more oligotrophic marine conditions and salinities (>35 psu) are implied by relatively low abundance of the r-selected opportunist *R. minuta* (Auer et al., 2014, 2015; Haq, 1980; Lohmann & Carlson, 1981) and the high abundance of small *Gephyrocapsa* sp., which is commonly associated with well stratified water masses in tropical and subtropical continental margin settings with salinities ~35 psu (Boeckel et al., 2006; Boeckel & Baumann, 2008; Bollmann, 1997; Okada & Honjo, 1973; Takahashi & Okada, 2000; Ziveri et al., 2004). The presence of warm oligotrophic (i.e., tropical) water masses is indicated by common *Umbilicosphaera sibogae* (Figures 2c and S3l), which today is present in the equatorial assemblages of the Indian and Pacific Ocean, and the hemi-pelagic regions off the coast of Australia (Baumann et al., 2016; Boeckel et al., 2006; Boeckel & Baumann, 2004, 2008; Guerreiro et al., 2005; Kinkel et al., 2000; Okada & Honjo, 1973; Young et al., 2017). This interpretation is supported by the presence of the upper photic zone species (<50-m water depth) *Umbellosphaera* spp. (Figure S3j), regarded as a classical tropical taxon in the modern ocean preferring warm to temperate oligotrophic open marine conditions (Boeckel et al., 2006; Boeckel & Baumann, 2004, 2008; Hagino & Okada, 2006; Kinkel et al., 2000; Okada & Honjo, 1973; Okada & Wells, 1997). The presence of common *Oolithotus* spp. (Andruleit, 2007; Boeckel et al., 2006; Boeckel & Baumann, 2004, 2008; Gartner, 1972; Young et al., 2017) further supports the interpretation that stratified water masses persisted during the deposition of TG1 (Figure S3e).

Taphogroup 2 (TG2) is defined as a eutrophic to mesotrophic assemblage by the common occurrence of medium sized reticulofenestrids *R. haqii* and *R. antarctica* (Figures 2e and S3h), generally associated with neritic environmental conditions and elevated nutrient conditions associated with locally confined upwelling (Auer et al., 2014, 2015; Haq & Lohmann, 1976; Lohmann & Carlson, 1981; Wade & Bown, 2006). *Reticulofenestra antarctica* is documented to favor elevated nutrient conditions in relatively shallow waters by Wade and Bown (2006). Less stable environmental conditions with potentially seasonally fluctuating temperature, salinity, and/or nutrient levels are implied by the increased abundance of the opportunistic (r-selected) *R. minuta* (Figure S3g), able to proliferate in highly variable environmental conditions (Auer et al., 2014, 2015; Lohmann & Carlson, 1981; Wade & Bown, 2006). Relatively cooler and nutrient enriched intermediate water masses potentially including Sub-Antarctic Mode Water (SAMW; see Text S1) are implied by the increased abundance and continuous occurrence of *Calcidiscus leptoporus* subsp. small (Figure S3b). Today the small morphotype of *Calcidiscus leptoporus* exhibits broad ecological adaption with a possible affinity for cool subpolar water masses and elevated nitrate levels in its preferred habitat between 50- and 100-m water depth (Baumann et al., 2016; Boeckel et al., 2006; Boeckel & Baumann, 2004, 2008; Cachão & Moita, 2000; Ferreira & Cachão, 2005; Hagino & Okada, 2006; Knappertsbusch, 1993; Renaud et al., 2002; Ziveri et al., 2004).

Taphogroup 3 (TG3) is dominated by *R. minuta* (Figure S3g) indicating neritic waters rich in terrigenous nutrients and environmental conditions favoring r-selected opportunists (Auer et al., 2014, 2015; Haq & Lohmann, 1976; Lohmann & Carlson, 1981; Wade & Bown, 2006). Common but discontinuous occurrence of *C. leptoporus* subsp. small (see above; Figure S3b) hints at cooler water masses reaching the intermediate photic zone than in TG1 but generally warmer than in TG2. This is also supported by the low occurrence of *R. antarctica* and *R. haqii* (Figure S3h), two species favoring environments with elevated upwelling-derived nutrient levels. TG3 is consequently regarded as reflecting highly variable environmental conditions with variable surface water temperatures and/or salinity levels coupled with potentially significant nutrient influx from the hinterland.

4.2. The Relationship Between C/S Ratio and Water Column Mixing

A comparison of the C/S ratio and $\delta^{18}O_{T.\ sacculifer}$ values at Site U1463 shows a strong coevolution of the two data sets between 3.5 and 3.0 Ma (Figures 3c and 4c). The beginning of this covariation coincides with the start of a noticeable SST drop and $\delta^{18}O_{ivc\text{-}sw}$ rise (local sea surface salinity decrease) recorded at Site 763

(Karas et al., 2011b), indicating that C/S values at Site U1463 were affected by paleoenvironmental changes which occurred along the NWS. These changes closely coincide with a distinct subsurface water cooling at Site 214 (Figure 3a), which Karas et al. (2009) relate to a switch in dominant ITF water masses from central Pacific to more northern Pacific regions (Karas et al., 2009, 2011b).

To explain this covariation, we consider the C/S ratio to be reflective of changes in the fixation sulfur (i.e., pyritization) compared to the overall availability of organic matter within the sediment water interface (e.g., Berner & Raiswell, 1983, 1984; Morse & Berner, 1995; Sagemann et al., 1999). The C/S ratio is thus strongly related to the prevailing redox conditions within the sediment and/or water column (Zou et al., 2012). Low C/S ratios are usually caused by increased water column stratification leading low oxygen concentrations at the sediment water interface, resulting in increased pyrite formation (= sulfur fixation) relative to organic matter burial (Berner & Raiswell, 1983; Morse & Berner, 1995; Sageman & Lyons, 2003). This relationship was documented in Holocene to Late Pleistocene samples spanning the last 48 ka in the Sea of Japan (Zou et al., 2012). Following the interpretation of Zou et al. (2012) we thus assume that increased (reduced) water turbulence leads to higher (lower) oxygenation at the sediment water interface. Increasing (decreasing) oxygenation would consequently decrease (increase) pyritization relative to organic matter consumption leading to an increase (decrease) in C/S values.

Changes in the Site U1463 C/S ratio together with significant contemporary changes in SSTs and SSS at Site 214 and 763A are thus likely related to a shift in prevailing water masses and/or ocean stratification as an effect of paleoceanographic changes along the NWS related to both ITF strength and local wind driven upwelling (Figures 1, 2, 5, and 6). Accepting this interpretation shows that although $\delta^{18}O_{T.\ sacculifer}$ values between 3.66 and 2.97 Ma are predominantly controlled by insolation driven changes in local SSTs at Site U1463 (De Vleeschouwer et al., 2018), a continuous decrease between 3.5–3.4 Ma can be directly linked to the proposed switch to northern Pacific ITF source waters rather than locally rising SSTs (Figure 4c).

4.3. Paleoenvironmental Model

Using the distribution of taphogroups over time, in combination with XRF riverine influx, dust flux proxies, and C/S ratio derived estimates of changes in water column stratification, allowed the definition of intervals reflective of changing paleoecological conditions (Figures 2, 4, and S3):

Interval 1 "Tropical ITF source mode" (312.84–302.74 m CCSF; 3.66–3.54 Ma): TG1 dominates this interval reflecting a tropical warm water masses in a neritic shelf setting. Common occurrence of open marine and warm oligotrophic shallow photic zone species *U. sibogae* and *Umbellosphaera* spp. indicates at least intermittently oligotrophic conditions. Interval 1 also exhibits an acme of small *Gephyrocapsa*, which also reflects a well-stratified (sub)tropical neritic setting (Figures 2a, 2b, and 2, 4, and S3). The rare, discontinuous occurrence of poorly preserved deep photic zone oligotrophic *Discoaster* spp. and the occurrence of *Oolithotus* spp. provides further support for the presence of well stratified water masses with moderately elevated nutrient conditions (Figure S3). This is corroborated by the presence of *Sphenolithus* spp. (Figures S3i and Table S5), although their global extinction ~3.51 Ma (Gibbs et al., 2005; Gradstein et al., 2012; Figure S3i) makes this taxon's use as a paleoecological indicator somewhat problematic. Its pattern of decline at Site U1463 toward 3.54 Ma nevertheless appears to have been linked to local paleoenvironmental changes and is thus likely also related to the proposed change in ITF source waters. The last occurrence of *Sphenolithus* spp. (relative abundance <1%) is subsequently recorded at 3.513 Ma at Site U1463.

The strong influence of open marine oligotrophic surface water in interval 1 is also reflected in the low C/S ratio (Figure 3c). C/S values suggest relatively low oxygen levels at the sediment water interface (Berner & Raiswell, 1983, 1984). High but decreasing values of terrigenous influx and low values of dust flux indicate generally high but continuous humidity in the hinterland of Australia (Figure 3d), during the final stages of the Australian humid interval (Christensen et al., 2017; Krebs et al., 2011). Dust flux varies only slightly between 3.66 to 3.54 Ma, likely indicating a relatively stable vegetation cover during the Australian Humid Interval (Figure 3e; Krebs et al., 2011). The decreasing humidity in Interval 1 was likely forced by the progressive uplift of the maritime continent creating a moisture barrier north of Australia (e.g., Christensen et al., 2017).
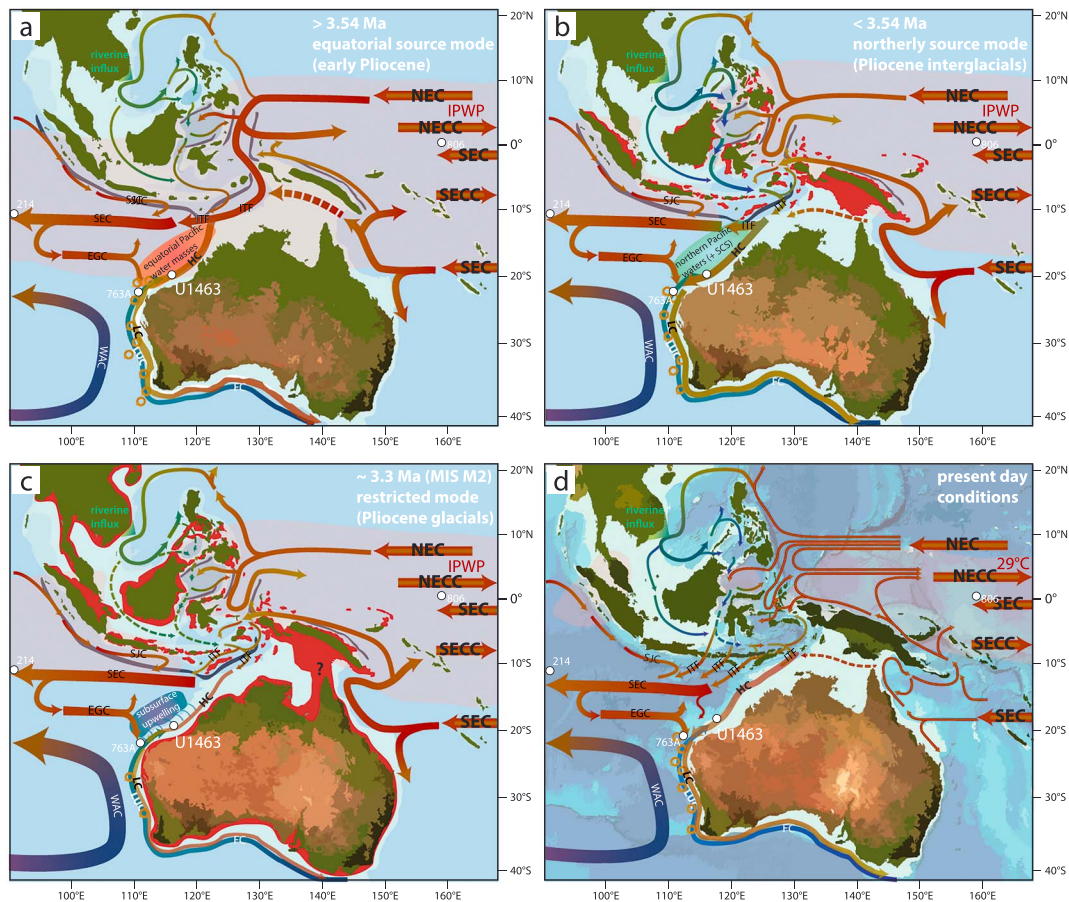
Figure 5. Tectonic and oceanographic change throughout the studied interval between 3.65 and 2.97 Ma. Tectonic maps are inferred by the data provided in Hall (2002). Current abbreviations follow the same scheme as in Figure 1. Red shaded ocean areas represent the theorized extend of the 29 °C isotherm in the Indo-Pacific Warm Pool (IPWP). (a) Map showing the proposed open equatorial connection between the Pacific and the Indian Ocean. Deep water exchange likely became restricted earlier by progressive restriction of the Halmahera straight and uplift of Halmahera after 5 Ma (Hall, 2002; Hall et al., 1988). The extent of northern vegetation is inferred from Krebs et al. (2011); (b) configuration with landmasses potentially above sea level after 3.54 Ma (Molnar & Cronin, 2015) shown in red. Deep blue lines indicate active subduction zones during the Pliocene (Hall, 2002, 2012). Uplift of Timor is implied by 3.5 Ma (Tate et al., 2017); closure of the Halmahera straight and uplift of Halmahera during this timeframe is implied by modeling data and field studies (Audley-Charles, 2011; Cane & Molnar, 2001; Godfrey, 1996; Gold et al., 2017; Hall, 2002; Hall et al., 1988; Kuhnt et al., 2004; Molnar & Cronin, 2015). Vegetation cover was reduced in this map to reflect lower riverine influx indicating reduced precipitation. Desertification remained weak; (c) throughflow geometry with the potentially maximum emergent land during marine isotope stage M2 (assuming a sea level lowstand of −30 m with modern-day shelf configuration of the Sunda and Sahul shelves). Aridification and reduced vegetation cover (after Krebs et al., 2011) reflects our riverine influx and dust flux records; (d) modern configuration (Figure 1) as a reference to compare the modern throughflow geometry to the proposed geometry changes between 3.65 and 2.97 Ma. NEC = North Equatorial Current; NECC = North Equatorial Counter Current; SEC = South Equatorial Current; SECC = South Equatorial Counter Current.

We interpret Interval 1 as reflecting a stage in the Pliocene tectonic ITF reorganization that still exhibited a strong connection to the equatorial Pacific (Figures 5a and 6a; Cane & Molnar, 2001; Christensen et al., 2017; Karas et al., 2009). These findings are supported by Nd isotopic studies indicating that a strong equatorial connection between the Indian and Pacific Oceans persisted until ~3.54 Ma (Gourlan et al., 2008; Le Houedec et al., 2012). This tropical ITF connection transported warm, oligotrophic, and saline equatorial Pacific waters to the eastern Indian Ocean, fueling a broad and very stable shallow water current of warm equatorial Pacific waters along the NWS. This equatorial ITF mode led to open marine conditions in the surface waters. Capping relatively cooler and nutrient-rich Indian Ocean waters this proto LC resulted in a comparatively well-stratified water column at Site U1463. The resultant strong and deep thermocline and nutricline enabled the proliferation of tropical, oligotrophic nannoplankton flora in the shallow to intermediate photic zone (0–100 m) at Site U1463 (Figures 5a and 6a). This mode is reflected in the Indian Ocean by high Mg/Ca temperatures and high $\delta^{18}O_{ivc\text{-}sw}$ values at Site 763A indicating the
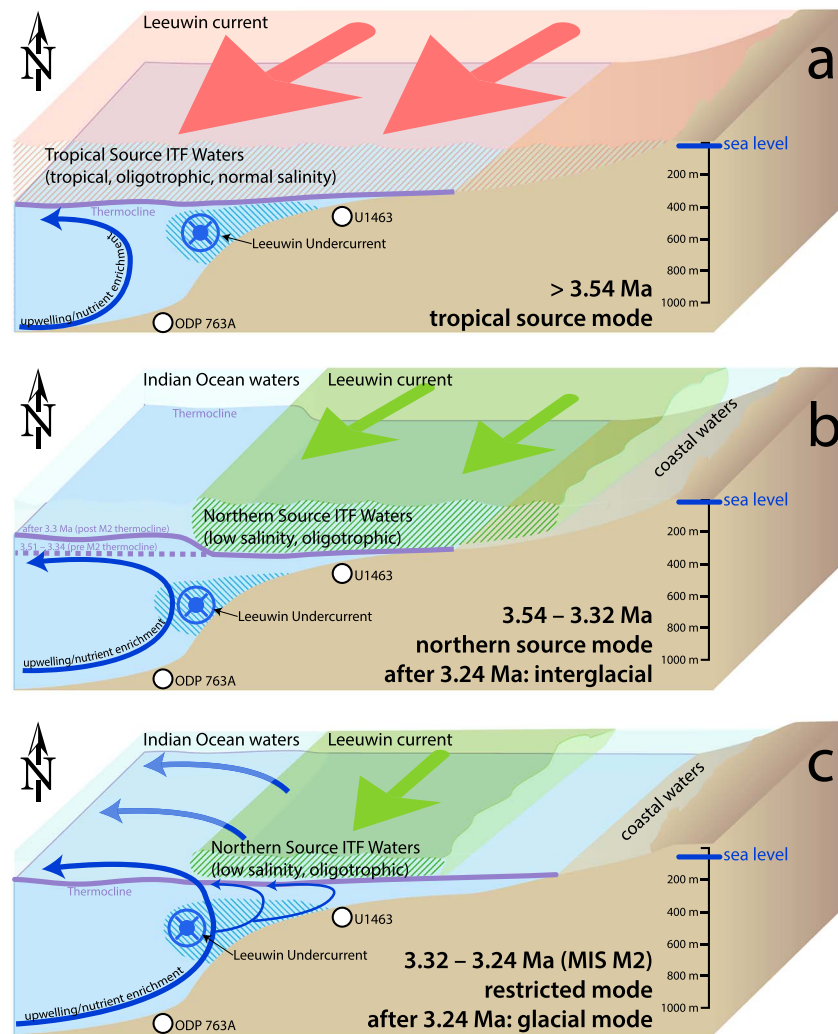
Figure 6. Conceptional oceanographic model along the Australian northwest shelf (NWS) reflecting the position of the Leeuwin Current (LC) in an idealized northeast-southwest transect between sites 763A and U1463. (a) Slope model shows the equatorial LC along the NWS inferred by nannofossil assemblage data and the paleogeographic configuration proposed in Figure 5a before 3.51 Ma. The proposed configuration explains an explanation for a relatively deep thermocline even during glacials along the NWS and suppressed upwelling through low along shore wind stress. (b) Slope model shows the proposed effect of northern mode Indonesian Throughflow (ITF) along the NWS between 3.51 and 3.34 Ma and interglacials after 3.3 Ma. An extensive low salinity cap dominates along the NWS being transported by a stronger and cooler ITF from northern sources in the South China Sea. Thermocline depth is slightly reduced but upwelling remains suppressed by the surface cap before 3.3 Ma (pink dashed line); after 3.3 Ma a much shallower thermocline persisted in the eastern Indian Ocean (pink solid line). (c) Slope model reflecting glacial lowstand restricted ITF first established during marine isotope stage (MIS) M2 (~3.3 Ma), significant sea level lowstand restricts connections to the North Pacific weakening the LC and allowing for stronger along shore winds and thus upwelling through the "Sahul-Indian Ocean Bjerknes" mechanism (Bjerknes, 1969; Di Nezio et al., 2016).

extension of these tropical Pacific surface waters further south along the NWS (Karas et al., 2011b; Karas et al., 2017) and also into the equatorial Indian Ocean at DSDP Site 214 (Karas et al., 2009; Karas et al., 2017).

Interval 2 "Transition to northern ITF source" (302.54–297.64 m CCSF; 3.54–3.46 Ma). This interval represents a departure from the tropical assemblage components of TG1 present in Interval 1 and is characterized by alternating TG2 and TG3. In addition to the extinction of *Sphenolithus* spp. recorded at 3.513 Ma at Site U1463, the beginning of Interval 2 also marks the disappearance of common *U. sibogae* (Figures S3l and 2c) and increasing occurrence of the mesotrophic taxa *Helicosphaera* spp. and *Umbilicosphaera jafari* (+ *U. foliosa*; Figures S3d and S3k). Coupled with a drop in *H′* diversity and species evenness (Figures S3m and

S3n), these assemblage shifts indicate a significant change from oligotrophic to more mesotrophic conditions. This shift falls together with the abrupt end of the small *Gephyrocapsa* dominance (Figure S3c) and a continuous increase of *R. minuta* (Figure S3g). It is important to note that the end of this Pliocene *Gephyrocapsa* acme displays a widely diachronous occurrence as shown by several globally distributed records (Ballegeer et al., 2012; Gibbs et al., 2004, 2005; Marino & Flores, 2002). Our data thus lend further support to the interpretation proposed by Ballegeer et al. (2012) that the small *Gephyrocapsa* acme represents a response to decreases in local water column stratification during the Pliocene.

The increase in deeper dwelling (50–100 m) *C. leptoporus* subsp. small during Interval 2 (Figures S3b and 4f) may indicate a stronger influence of SAMW unrelated to a major global glaciation and/or sea level lowstand (Lisiecki & Raymo, 2005; Miller et al., 2012). This may hint at a shallowing of the LC at Site U1463 at this time (Figures 2 and 4e). Increasing nutrient availability and thus increasing water column mixing is also reflected by the increased abundance of medium sized reticulofenestrids *R. haqii* and *R antarctica* (Figure S3h) and a proliferation of the more nutrient-adapted *U. jafari* and *U. foliosa* (Figure S3k), together with an increase of opportunistic generalists such as *Helicosphaera* spp. (Baumann et al., 2005; Boeckel & Baumann, 2004, 2008; Ferreira & Cachão, 2005; Okada & Honjo, 1973; Takahashi & Okada, 2000; Ziveri et al., 2004; Figure S3d and Table S2).

Site 763A also shows decreasing SSTs between 3.52 and 3.40 Ma (Karas et al., 2011b; Karas et al., 2017). Here decreasing SSSs indicated by $\delta^{18}O_{ivc-sw}$ (Figure 3b), in line with the C/S ratio trends at Site U1463 (Figure 3c), suggest that the switch to cooler low-salinity waters around 3.5 Ma had a pronounced effect on the NWS paleoenvironment. Site 214 (Karas et al., 2009) shows decreasing *G. ruber/T. sacculifer* and *G. crassaformis* Mg/Ca temperatures after 3.5 Ma (Figure 4a), suggesting that changing surface and intermediate water temperatures and potentially salinity levels in the ITF are the main driving factor for the recorded changes between Interval 1 and 2 (Figures 2, 4, and 5). Overall high $\delta^{18}O_{G.\ crassaformis}$ values at Site 214 between 3.6 and 3.3 Ma (Karas et al., 2009) further support this change in ITF source waters (Figure 4b).

We therefore interpret Interval 2 at Site U1463 to reflect increasing "northern ITF source waters" from the north Pacific as indicated by decreasing SST at Site 763 after 3.54 Ma. This interpretation is in line with the proposed closure and/or restriction of the equatorial Pacific ITF pathway due to the uplift of Halmahera and closure of the Halmahera strait (Godfrey, 1996; Gold et al., 2017; Hall, 2002; Hall et al., 1988; Kuhnt et al., 2004; Molnar & Cronin, 2015; Wijeratne et al., 2018; Figures 2, 3, and 5b). This led to a possibly narrower LC, similar to its modern configuration, with more turbulent flow and stronger LC eddy formation (Waite et al., 2007). This changed LC resulted in stronger water column mixing and a shallower thermocline and nutricline at Site U1463, which is well supported by the observed nannofossil assemblage changes. Precipitation on the Australian continent reduced further during Interval 2, reflecting the latest stages of the Humid Interval (Christensen et al., 2017), and is also reflected by slightly increased but still relatively low influx of windblown dust at Site U1463 (Figures 3e).

Interval 3 "Northern ITF source mode" (291.13–297.44 m CCSF; 3.46–3.32 Ma): An acme of *R. minuta* (Figures 2a and S3g) at Site U1463 during Interval 3 reflects paleoenvironmental conditions favoring r-selected opportunists (= TG3), which cope well in changing neritic environmental conditions. Most open marine and tropical nannofossil species occur only intermittently as minor and accessory parts of the assemblage (Figures 2c and S3g). We thus regard Interval 3 as reflecting a fully reconfigured ITF transporting relatively cooler waters from the northern Pacific into the Indian Ocean (Figures 5b and 6b). This is also reflected by high C/S values at Site U1463 and further dropping $\delta^{18}O_{ivc-sw}$ values and decreasing temperatures at Site 763 (Karas et al., 2011b). After ~3.4 Ma a drop in $\delta^{18}O_{T.\ sacculifer}$ values at Site 763 (Karas et al., 2011b) compared to Site U1463 (De Vleeschouwer et al., 2018) reflects decreasing ITF influence farther south (Figure 4a), starting with increase in global ice volume following isotope stage MG4 (Lisiecki & Raymo, 2005). Terrigenous input and dust flux remain constant during Interval 3 reflecting stable climatic conditions on the Australian hinterland at the end of the Australian Humid Interval.

Interval 4 "M2 event glacial ITF mode" (290.74–287.54 m CCSF; 3.32–3.24 Ma): A dominance of TG2 in this interval reflects cool, nutrient-rich intermediate water masses and/or SAMW from the Indian Ocean reaching Site U1463 during the MIS M2 glacial event. An increase in *C. leptoporus* subsp. small indicates an

increased influence of relatively cooler (= SAMW) nutrient-rich intermediate waters via the Leeuwin Undercurrent in its habitat between 50- and 100-m water depth. This is supported by a strong increase in *R. antarctica* adapted to nutrient-rich conditions with low freshwater input (Wade & Bown, 2006). Together with stable isotopic values (De Vleeschouwer et al., 2018), these results show that while the LC and thus ITF never ceased during the M2 glacial event, the flow along the NWS constricted allowing a stronger influence of open Indian Ocean waters at Site U1463 via subsurface upwelling (e.g., De Vleeschouwer et al., 2018). Today, a weaker LC reduces the warm-water and low-density cap along the NWS allowing prevailing westward winds to increase Ekman transport and consequently (subsurface-) upwelling (D'Adamo et al., 2009; Ridgway & Godfrey, 2015; Thompson et al., 2011; Waite et al., 2007; Wijeratne et al., 2018; Zhang et al., 2016).

Similar weak or subsurface upwelling was observed to significantly impact nannofossil assemblages along the LC over the last 30 kyr (Takahashi & Okada, 2000), indicating that the LC showed a similar response during the M2 event as during the last glacial maximum (Figures 5c and 6c). Interval 4 thus represents a response of nannoplankton assemblages to weaker and more restricted ITF waters flowing along the shelf areas during cooler austral autumn and winters (Bahmanpour et al., 2016; Rousseaux et al., 2012; Wijeratne et al., 2018). Such a reduced LC would allow for intermittent subsurface upwelling, caused by increased wind shear and a weakened warm, low-salinity, surface water cap, leading to a shallower mixed layer (Rousseaux et al., 2012; Figures 5c and 6c). The termination of Interval 4 coincides with the transgression associated with MIS M1 (Lisiecki & Raymo, 2005; Miller et al., 2012). This sea level highstand also marks the termination of the ~0.5 ‰ offset between the isotopic values of site 763 and U1463 (De Vleeschouwer et al., 2018), indicating that the LC again reached Site 763A by ~3.2 Ma. These results imply a link between the observed paleooceanographic changes and the end of the Australian Humid Interval and the beginning of the Transitional Interval at 3.3 Ma (Andrae et al., 2018; Christensen et al., 2017; Di Nezio et al., 2016; Krebs et al., 2011; Sniderman et al., 2016)

Interval 5 "*Post M2 glacial/interglacial ITF mode*" (287.44–277.84 m CCSF; 3.23–2.97 Ma): the final interval reflects the response of local oceanographic conditions to increased glacial/interglacial amplitudes and seasonality after MIS M2 (De Vleeschouwer et al., 2018; Lisiecki & Raymo, 2005). TG2 and TG3 alternate on an orbital scale showing cooler and more open marine TG2 dominantly occurring during ETP maxima in glacial times (Figures 4c and 4e). In particular, the glacial intervals KM2, K2, G22, and G20 (Figure 4e) reflect the response of the LC and ITF to increased effects of glacio-eustatic variability in the Indian Ocean after MIS M2. The strong response of the LC to MIS KM4 and MIS K2 also suggests that comparatively small sea level drops (~20–30 m; Miller et al., 2012) sufficiently altered the path of the LC along the NWS following MIS M2 (e.g., Di Nezio et al., 2016). Stronger upwelling is also implied by the $\delta^{13}C_{T.\ sacculifer}$ data of De Vleeschouwer et al. (2018) during MIS KM4 (~3.2 Ma; Figures 4d). Both $\delta^{13}C_{T.\ sacculifer}$ and classical glacial indicators like *Pseudoemiliania* spp. (see Gartner, 1972) show a strong precessional pacing imparted on long-term orbital variability (Figures 4c–4e). Overall, our nannofossil assemblages thus indicate a stronger response of upwelling sensitive taxa during glacials than in interglacials (Figures 2d, 2e, 4d, and 4e). This interpretation is in line with modeling studies (Di Nezio et al., 2016). Their study suggests that sea level drops around 30 m are enough to significantly alter the hydroclimatic conditions along northwest Australia, leading to stronger upwelling and reduced humidity via the Sahul-Indian Ocean Bjerknes mechanism with an increased east-west tilt of the Indian Ocean thermocline. In summary, it appears that the heightened glacial/interglacial variability after 3.3 Ma resulted in oceanographic conditions along the NWS that were already comparable to its proposed Pleistocene configuration implying a stronger ITF and Leeuwin current during interglacials and a weaker ITF during glacials leading to increased seasonal upwelling of cool nutrient-rich water masses of the Leeuwin Undercurrent (Gallagher et al., 2009; Godfrey & Mansbridge, 2000; Ridgway & Godfrey, 2015; Spooner et al., 2011; Wijeratne et al., 2018).

Around MIS G20 (~3.0 Ma) a drop in C/S values (Figure 3c) also suggests a re-establishment of more stratified water conditions along the NWS, suggesting an at least seasonally reduced LC, supported by r-selected opportunists (Figure 2a) and potentially dropping SSTs shown by increased $\delta^{18}O_{T.\ sacculifer}$ values (Figure 4c; De Vleeschouwer et al., 2018). Interestingly, G20 is also noted as a distinct change in the subtropical front in the Tasman Sea resulting in the end of the *small Gephyrocapsa* acme at Site 590 (Ballegeer et al., 2012). The authors relate this assemblage change to a significant shift in the dominant waters masses reaching Tasmania and link it to the intensification of the atmospheric circulation related to late Pliocene climate

cooling causing an increased equator to pole heat gradient (Ballegeer et al., 2012). Combined with strong evidence pointing toward enhanced Southern Hemisphere cooling (Lisiecki & Raymo, 2005; Riesselman & Dunbar, 2013), this indicates a further significant equatorward expansion of cool Antarctic water masses at that time as a likely explanation for the observed SST drop at Site U1463.

Australian climate shows a variable pattern during interval 5 spanning the first ~300 kyr of the Transitional Interval after MIS M2 (Figure 3d). These variable conditions in northern Australia during the Transitional Interval may be related to sea level-driven fluctuations in the Indian Ocean Bjerknes mechanism and/or changes in the Australian Monsoon system, resulting in more seasonal precipitation during Austral Summer and reduced aridity in winter during stronger interglacials like KM3 (Figures 3d and 4e). A link to a globally changing monsoon system is also supported by a contemporary strengthening of the East Asian Summer Monsoon (Ao et al., 2016). After ~3.10 Ma, however, terrigenous flux at Site U1463 drops significantly, coupled with an increase in dust flux showing the inception of precession paced aridity patterns in Australia until the end of the studied interval ~2.97 Ma ago (Figure 3d).

4.4. Implications of Pliocene Indonesian Throughflow Restriction

Our multiproxy analysis suggests that a dominant connection between the central equatorial Pacific and the Indian Ocean persisted at least until 3.54 Ma, when a threshold in the tectonic configuration of the Indonesian Archipelago was reached, resulting in a switch in dominant ITF pathways (e.g., Cane & Molnar, 2001). This initial reconfiguration drastically altered oceanographic conditions (temperature, water stratification, and nutrient levels) along the NWS leading to a pronounced decline of tropical, oligotrophic nannoplankton taxa at Site U1463 (Figures 2b and 2c, and S3). This shift supports the hypothesis that tectonic ITF reconfiguration significantly reduced equatorial heat transport from the IPWP into to the Indian Ocean, in line with previous studies (Cane & Molnar, 2001; Karas et al., 2009; Karas et al., 2017; Molnar & Cronin, 2015). Our data further indicate that this initial tectonically forced restriction during the Pliocene did not necessarily restrict total throughflow volume but rather changed the dominant water sources to cooler and lower-salinity waters from the northern Pacific and the SCS (Cane & Molnar, 2001; De Vleeschouwer et al., 2018; He et al., 2015; Karas et al., 2009, 2011b). The tectonic ITF reorganization postdates increases in East Asian Summer Monsoon strength by at least 100 kyr (Ao et al., 2016), showing that the observed shift in ITF waters ~3.54 Ma was likely not directly caused by monsoon-related discharge into the South China Sea (e.g., Kuhnt et al., 2004).

A comparison of $\delta^{18}O_{T.\ sacculifer}$ records from sites U1463 and 763A (De Vleeschouwer et al., 2018) already suggested that LC dynamics were affected by a long-term global sea level lowstand between ~3.4 and 3.2 Ma resulting in Site 763A temporarily falling outside the direct influence of the LC (De Vleeschouwer et al., 2018; Miller et al., 2012). The recorded assemblage changes (Figures 2 and S3), and contemporary drop in equatorial Indian ocean surface and thermocline SSTs at Site 214 (Karas et al., 2009; Figures 4a and 4c) ~3.5 Ma now confirm that significant changes in ITF source waters clearly preceded the isotopic offset between Site U1463 and 763A by ~140 kyr (De Vleeschouwer et al., 2018).

The up to ~60-m regression during MIS M2 (Miller et al., 2012) may have exposed significant Australian Shelf areas for the first time (Figure 5c). MIS M2 was thus possibly the first time during the Pliocene that Australian shelf exposure reached a critical threshold needed to fully establish the Sahul-Indian Ocean Bjerknes mechanism (Bjerknes, 1969; Di Nezio et al., 2016). The Sahul-Indian Ocean Bjerknes mechanism would have led to anomalous easterlies coupled with a high-pressure cell forcing dry conditions in northern Australia for the first time (Figure 3d) and also forcing thermocline shoaling and upwelling in the eastern Indian Ocean during MIS M2 (Figures 2, 4, 5c, and 6c). This is supported by an increase in upwelling adapted nannoplankton taxa and the increase in $\delta^{13}C_{T.\ sacculifer}$ at Site U1463, which both indicate progressively increasing (sub)surface upwelling along the NWS after 3.3 Ma. Nevertheless, our nannofossil assemblage data and $\delta^{13}C_{T.\ sacculifer}$ data (De Vleeschouwer et al., 2018) also imply the LC returned to an at least seasonally strong mode transporting ITF waters along the NWS following the transgression associated with MIS M1 (Figures 2, 4d, and 4e). This reinvigorated ITF also strengthened the LC enough for LC eddy to again reach Site 763 by 3.2 Ma (De Vleeschouwer et al., 2018; Karas et al., 2011b). This strong but seasonally variable LC is likely the effect of a stronger steric height gradient forcing the LC along the NWS after temperature and salinity gradients increased between the Indonesian Seaways and the south eastern Indian Ocean (D'Adamo et al., 2009; Furue et al., 2017; Gordon et al., 2003; Wijeratne et al., 2018), resulting in a LC much

closer to its later Pleistocene configuration (Gallagher et al., 2009; Spooner et al., 2011). We thus propose that the reduced equatorial Pacific intermediate water component flowing into the Indian Ocean after ITF reconfiguration ~3.54 Ma was unable to warm the eastern Indian Ocean enough to reverse the east-west tilt of the Indian Ocean thermocline that formed between 3.4 and 3.3 Ma (Figures 2, 5, and 6). After MIS M2 this permanently tilted thermocline also made the equatorial Indian Ocean more susceptible to seasonality driven subsurface upwelling during glacials and weaker ITF (Figures 5d and 6c). This model would explain both the stronger glacial/interglacial variability after MIS M2 in our nannofossil records and by extent also the isotopic offset between Site U1463 and 763A (De Vleeschouwer et al., 2018).

While it has been established that the long-term history of Australian hydroclimate during the Pliocene was linked to the uplift of the Maritime Continent by shifting control of Australian climate from the Pacific to the Indian Ocean (Christensen et al., 2017), a clear constraint for this shift was missing until now. Our results now confirm this shift occurred at MIS M2, when a combination of ITF restriction, Indian Ocean cooling, and shelf exposure increased wind shear and thermocline shoaling, establishing an early form of the Bjerknes mechanism in the eastern Indian Ocean. Crucially, a fully established Sahul-Indian Ocean Bjerknes mechanism by MIS M2 also provides a clear process based hypothesis able to explain observed changes in African precipitation patterns and Mediterranean outflow during the Late Pliocene via the teleconnection proposed by Sarnthein et al. (2017).

5. Conclusions

Our sub-Milankovitch scale calcareous nannofossil and geochemical records from IODP Site U1463 combined with existing Indo-Pacific data (De Vleeschouwer et al., 2018; Karas et al., 2009, 2011b; Wara et al., 2005) enabled us to reconstruct the timing and pacing of tectonic ITF restriction during the Pliocene (3.66–2.97 Ma). The position of IODP Site U1463 within the upper branch of the LC provides new insights into Pliocene ITF dynamics between 3.66 and 2.97 Ma, allowing us to distinguish changes caused by tectonic ITF restriction from those imparted by global sea level variability, along the NWS:

1. The dominant equatorial connection between the Indo-Pacific Warm Pool and the Indian Ocean via the Indonesian Gateway had already ceased ~3.54 Ma, as shown by a distinct shift in nannofossil assemblages at Site U1463. These changes are in line with cooling equatorial Indian Ocean temperatures at Site 214, pinpointing the switch to dominant northern Pacific ITF sources for the first time.
2. Nannofossil assemblages provide detailed insights into how initial ITF reorganization after 3.5 Ma led to fundamental changes in paleoenvironmental conditions along the NWS and altered LC dynamics: The northern mode ITF led to a weakening or at least constriction of the LC, resulting in Site 763A, further offshore and downstream of the LC, reflecting a more open Indian Ocean signal, which became especially pronounced during a long-term sea level lowstand between 3.4 and 3.2 Ma.
3. The MIS M2 glaciation at 3.3 Ma was amplified by a significant reduction in equatorial heat exchange between the Pacific and Indian Ocean after 3.5 Ma. During MIS M2 sea level driven ITF restriction further enhanced the observed thermal isolation of Antarctica (De Vleeschouwer et al., 2018; Patterson et al., 2014) leading to the irreversible cooling of the eastern Indian Ocean (Karas et al., 2009, 2011b) and Antarctica (Riesselman & Dunbar, 2013) from 3.3 Ma onward.
4. Nannofossil assemblage and $\delta^{13}C_{T.\ sacculifer}$ data show that the Pliocene sea level lowstand culminating in MIS M2 (Miller et al., 2012) likely established an early form of the Sahul-Indian Ocean Bjerknes mechanism leading to upwelling along the NWS (Di Nezio et al., 2016). This mechanism also enhanced seasonality and aridification on the Australian Continent after 3.3 Ma, by establishing a more seasonally variable LC (Godfrey & Mansbridge, 2000; Ridgway & Godfrey, 2015; Wijeratne et al., 2018).
5. The permanently tilted thermocline by 3.3 Ma and heightened glacial/interglacial LC variability after ~3.2 Ma resulted in oceanographic conditions along the NWS that were much closer to their Pleistocene configuration characterized by a weaker (stronger) LC during glacials (interglacials) (Gallagher et al., 2009; Spooner et al., 2011). These insights also illustrate the significant role eastern Indian Ocean surface water conditions played during the inception of the Australian Transitional Interval (Christensen et al., 2017).

This study thus provides a unique time series of Pliocene paleoenvironmental conditions along the northwest shelf of Australia while linking them with long-term changes in Australian climate. The observed local

paleoenvironmental and paleoclimatological changes corroborate well-established conceptual models of Indian Ocean and Australian Climate dynamics. Combined, this resulted in a robust model tying local environmental changes on the NWS to global Pliocene climatic trends. Our results also provide strong support for the interhemispheric teleconnection proposed by Sarnthein et al. (2017). We show the direct effect of changing ITF dynamics, especially in relation to changing sea level, had on past Australian and also global climatic changes.

References

Anand, P., Elderfield, H., & Conte, M. H. (2003). Calibration of Mg/Ca thermometry in planktonic foraminifera from a sediment trap time series. *Paleoceanography*, *18*(2), 1050. https://doi.org/10.1029/2002PA000846

Andrae, J. W., McInerney, F. A., Polissar, P. J., Sniderman, J. M. K., Howard, S., Hall, P. A., & Phelps, S. R. (2018). Initial expansion of C4 vegetation in Australia during the Late Pliocene. *Geophysical Research Letters*, *19*, 171. https://doi.org/10.1029/2018GL077833

Andruleit, H. (2007). Status of the Java upwelling area (Indian Ocean) during the oligotrophic northern hemisphere winter monsoon season as revealed by coccolithophores. *Marine Micropaleontology*, *64*(1-2), 36–51. https://doi.org/10.1016/j.marmicro.2007.02.001

Ao, H., Roberts, A. P., Dekkers, M. J., Liu, X., Rohling, E. J., Shi, Z., et al. (2016). Late Miocene–Pliocene Asian monsoon intensification linked to Antarctic ice-sheet growth. *Earth and Planetary Science Letters*, *444*, 75–87. https://doi.org/10.1016/j.epsl.2016.03.028

Aubry, M.-P. (1984). *Handbook of Cenozoic calcareous nannoplankton: Book 1. Ortholithae (discoasters)*. New York: Micropaleontology Press.

Aubry, M.-P. (1988). Handbook of Cenozoic Calcareous Nannoplankton: Book 2. Ortholithae (Holococcoliths, 697 Ceratoliths, Ortholiths and Others). New York: Micropaleontology Press.

Aubry, M.-P. (1989). *Handbook of Cenozoic calcareous nannoplankton: Book 3. Ortholithae (Pentaliths, and others), Heliolithae (Fasciculiths, Sphenoliths and others)*. New York: Micropaleontology Press.

Aubry, M.-P. (1990). *Handbook of Cenozoic calcareous nannoplankton: Book 4. Heliolithae (Helicoliths, Cribriliths, Lopadoliths and others)*. New York: Micropaleontology Press.

Aubry, M.-P. (1999). *Handbook of Cenozoic calcareous nannoplankton. Book 5: Heliolithae (Zygoliths and Rhabdoliths)*. New York: Micropaleontology Press.

Audley-Charles, M. G. (2011). Tectonic post-collision processes in Timor. *Geological Society, London, Special Publications*, *355*(1), 241–266. https://doi.org/10.1144/SP355.12

Auer, G., Piller, W. E., & Harzhauser, M. (2014). High-resolution calcareous nannoplankton palaeoecology as a proxy for small-scale environmental changes in the Early Miocene. *Marine Micropaleontology*, *111*, 53–65. https://doi.org/10.1016/j.marmicro.2014.06.005

Auer, G., Piller, W. E., & Harzhauser, M. (2015). Two distinct decadal and centennial cyclicities forced marine upwelling intensity and precipitation during the late Early Miocene in central Europe. *Climate of the Past*, *11*(2), 283–303. https://doi.org/10.5194/cp-11-283-2015

Bahmanpour, M. H., Pattiaratchi, C., Wijeratne, E. M. S., Steinberg, C., & D'Adamo, N. (2016). Multi-year observation of Holloway Current along the shelf edge of North Western Australia. *Journal of Coastal Research*, *75*(sp1), 517–521. https://doi.org/10.2112/SI75-104.1

Ballegeer, A.-M., Flores, J. A., Sierro, F. J., & Andersen, N. (2012). Monitoring fluctuations of the Subtropical Front in the Tasman Sea between 3.45 and 2.45 Ma (ODP site 1172). *Palaeogeography, Palaeoclimatology, Palaeoecology*, *313–314*, 215–224. https://doi.org/10.1016/j.palaeo.2011.11.001

Baumann, K.-H., Andruleit, H., Böckel, B., Geisen, M., & Kinkel, H. (2005). The significance of extant coccolithophores as indicators of ocean water masses, surface water temperature, and palaeoproductivity: A review. *Paläontologische Zeitschrift*, *79*(1), 93–112. https://doi.org/10.1007/BF03021756

Baumann, K.-H., Saavedra-Pellitero, M., Böckel, B., & Ott, C. (2016). Morphometry, biogeography and ecology of Calcidiscus and Umbilicosphaera in the South Atlantic. *Revue De Micropaléontologie*, *59*(3), 239–251. https://doi.org/10.1016/j.revmic.2016.03.001

Bemis, B. E., Spero, H. J., Bijma, J., & Lea, D. W. (1998). Reevaluation of the oxygen isotopic composition of planktonic foraminifera: Experimental results and revised paleotemperature equations. *Paleoceanography*, *13*(2), 150–160. https://doi.org/10.1029/98PA00070

Berner, R. A., & Raiswell, R. (1983). Burial of organic carbon and pyrite sulfur in sediments over phanerozoic time: A new theory. *Geochimica et Cosmochimica Acta*, *47*(5), 855–862. https://doi.org/10.1016/0016-7037(83)90151-5

Berner, R. A., & Raiswell, R. (1984). C/S method for distinguishing freshwater from marine sedimentary rocks. *Geology*, *12*(6), 365–368. https://doi.org/10.1130/0091-7613(1984)12<365:CMFDFF>2.0.CO;2

Bjerknes, J. (1969). Atmospheric teleconnections from the equatorial Pacific. *Monthly Weather Review*, *97*(3), 163–172. https://doi.org/10.1175/1520-0493(1969)097<0163:ATFTEP>2.3.CO;2

Boeckel, B., & Baumann, K.-H. (2004). Distribution of coccoliths in surface sediments of the south-eastern South Atlantic Ocean: Ecology, preservation and carbonate contribution. *Marine Micropaleontology*, *51*(3–4), 301–320. https://doi.org/10.1016/j.marmicro.2004.01.001

Boeckel, B., & Baumann, K.-H. (2008). Vertical and lateral variations in coccolithophore community structure across the subtropical frontal zone in the South Atlantic Ocean. *Marine Micropaleontology*, *67*(3-4), 255–273. https://doi.org/10.1016/j.marmicro.2008.01.014

Boeckel, B., Baumann, K.-H., Henrich, R., & Kinkel, H. (2006). Coccolith distribution patterns in South Atlantic and Southern Ocean surface sediments in relation to environmental gradients. *Deep-Sea Research Part I. Oceanographic Research Papers*, *53*(6), 1073–1099. https://doi.org/10.1016/j.dsr.2005.11.006

Bollmann, J. (1997). Morphology and biogeography of Gephyrocapsa coccoliths in Holocene sediments. *Marine Micropaleontology*, *29*(3–4), 319–350. https://doi.org/10.1016/S0377-8398(96)00028-X

Bordiga, M., Bartol, M., & Henderiks, J. (2015). Absolute nannofossil abundance estimates: Quantifying the pros and cons of different techniques. *Revue De Micropaléontologie*, *58*(3), 155–165. https://doi.org/10.1016/j.revmic.2015.05.002

Bray, J. R., & Curtis, J. T. (1957). An ordination of the upland forest communities of southern Wisconsin. *Ecological Monographs*, *27*(4), 325–349. https://doi.org/10.2307/1942268

Brierley, C. M., & Fedorov, A. V. (2011). Tidal mixing around Indonesia and the Maritime continent: Implications for paleoclimate simulations. *Geophysical Research Letters*, *38*, L24703. https://doi.org/10.1029/2011GL050027

Brigham-Grette, J., Melles, M., Minyuk, P., Andreev, A., Tarasov, P., DeConto, R., et al. (2013). Pliocene warmth, polar amplification, and stepped Pleistocene cooling recorded in NE Arctic Russia. *Science*, *340*(6139), 1421–1427. https://doi.org/10.1126/science.1233137

Cachão, M., & Moita, M. T. (2000). *Coccolithus pelagicus*, a productivity proxy related to moderate fronts off Western Iberia. *Marine Micropaleontology*, *39*(1–4), 131–155. https://doi.org/10.1016/S0377-8398(00)00018-9

Cachão, M., Oliveira, A., & Vitorino, J. (2000). Subtropical winter guests, offshore Portugal. *Journal of Nannoplankton Research*, *22*, 19–26.

Cane, M. A., & Molnar, P. (2001). Closing of the Indonesian seaway as a precursor to east African aridification around 3–4 million years ago. *Nature*, *411*(6834), 157–162. https://doi.org/10.1038/35075500

Christensen, B. A., Renema, W., Henderiks, J., De Vleeschouwer, D., Groeneveld, J., Castañeda, I. S., et al. (2017). Indonesian Throughflow drove Australian climate from humid Pliocene to arid Pleistocene. *Geophysical Research Letters*, *44*, 6914–6925. https://doi.org/10.1002/2017GL072977

Couapel, M. J. J., Beaufort, L., Jones, B. G., & Chivas, A. R. (2007). Late Quaternary marginal marine palaeoenvironments of northern Australia as inferred from cluster analysis of coccolith assemblages. *Marine Micropaleontology*, *65*(3–4), 213–231. https://doi.org/10.1016/j.marmicro.2007.07.006

D'Adamo, N., Fandry, C., Buchan, S., & Domingues, C. (2009). Northern sources of the Leeuwin Current and the "Holloway Current" on the North West Shelf. *Journal of the Royal Society of Western Australia*, *92*(2), 53–66.

De Deckker, P. (2016). The Indo-Pacific Warm Pool: Critical to world oceanography and world climate. *Geoscience Letters*, *3*(1), 643. https://doi.org/10.1186/s40562-016-0054-3

De Schepper, S., Fischer, E. I., Groeneveld, J., Head, M. J., & Matthiessen, J. (2011). Deciphering the palaeoecology of Late Pliocene and Early Pleistocene dinoflagellate cysts. *Palaeogeography, Palaeoclimatology, Palaeoecology*, *309*(1–2), 17–32. https://doi.org/10.1016/j.palaeo.2011.04.020

De Schepper, S., Gibbard, P. L., Salzmann, U., & Ehlers, J. (2014). A global synthesis of the marine and terrestrial evidence for glaciation during the Pliocene Epoch. *Earth-Science Reviews*, *135*, 83–102. https://doi.org/10.1016/j.earscirev.2014.04.003

De Schepper, S., Groeneveld, J., Naafs, B. D. A., Van Renterghem, C., Hennissen, J., Head, M. J., et al. (2013). Northern Hemisphere glaciation during the globally warm early Late Pliocene. *PLoS ONE*, *8*(12), e81508. https://doi.org/10.1371/journal.pone.0081508

De Vleeschouwer, D., Auer, G., Smith, R., Bogus, K., Christensen, B., Groeneveld, J., et al. (2018). The amplifying effect of Indonesian Throughflow heat transport on Late Pliocene Southern Hemisphere climate cooling. *Earth and Planetary Science Letters*, *500*, 15–27. https://doi.org/10.1016/j.epsl.2018.07.035

De Vleeschouwer, D., Vahlenkamp, M., Crucifix, M., & Pälike, H. (2017). Alternating Southern and Northern Hemisphere climate response to astronomical forcing during the past 35 m.y. *Geology*, *45*(4), 375–378. https://doi.org/10.1130/G38663.1

Di Nezio, P. N., Timmermann, A., Tierney, J. E., Jin, F.-F., Otto-Bliesner, B., Rosenbloom, N., et al. (2016). The climate response of the Indo-Pacific warm pool to glacial sea level. *Paleoceanography*, *31*, 866–894. https://doi.org/10.1002/2015PA002890

Ehrmann, W., Seidel, M., & Schmiedl, G. (2013). Dynamics of Late Quaternary North African humid periods documented in the clay mineral record of central Aegean Sea sediments. *Global and Planetary Change*, *107*, 186–195. https://doi.org/10.1016/j.gloplacha.2013.05.010

Ferreira, J., & Cachão, M. (2005). Calcareous nannoplakton from the Guadiana Estuary and Algarve continental shelf (Southern Portugal): An ecological model. *Thalassas*, *21*(1), 35–44.

Furue, R., Guerreiro, K., Phillips, H. E., Julian, P., McCreary, J., & Bindoff, N. L. (2017). On the Leeuwin Current System and its linkage to zonal flows in the South Indian Ocean as inferred from a gridded hydrography. *Journal of Physical Oceanography*, *47*(3), 583–602. https://doi.org/10.1175/JPO-D-16-0170.1

Gallagher, S. J., Fulthorpe, C. S., Bogus, K., & the Expedition 356 Scientists (2017). *Indonesian Throughflow. Proceedings of the International Ocean Discovery Program, 356*. College Station, TX: International Ocean Discovery Program. https://doi.org/10.14379/iodp.proc.356.2017

Gallagher, S. J., Wallace, M. W., Li, C. L., Kinna, B., Bye, J. T., Akimoto, K., & Torii, M. (2009). Neogene history of the West Pacific Warm Pool, Kuroshio and Leeuwin currents. *Paleoceanography*, *24*, PA1206. https://doi.org/10.1029/2008PA001660

Gartner, S. (1972). Late Pleistocene calcareous nannofossils in the caribbean and their interoceanic correlation. *Palaeogeography, Palaeoclimatology, Palaeoecology*, *12*(3), 169–191. https://doi.org/10.1016/0031-0182(72)90058-2

Gibbs, S., Shackleton, N., & Young, J. (2004). Orbitally forced climate signals in mid-Pliocene nannofossil assemblages. *Marine Micropaleontology*, *51*(1-2), 39–56. https://doi.org/10.1016/j.marmicro.2003.09.002

Gibbs, S. J., Young, J. R., Bralower, T. J., & Shackleton, N. J. (2005). Nannofossil evolutionary events in the mid-Pliocene: An assessment of the degree of synchrony in the extinctions of *Reticulofenestra pseudoumbilicus* and *Sphenolithus abies*. *Palaeogeography, Palaeoclimatology, Palaeoecology*, *217*(1–2), 155–172. https://doi.org/10.1016/j.palaeo.2004.11.005

Gingele, F. X., & De Deckker, P. (2004). Fingerprinting Australia's rivers with clay minerals and the application for the marine record of climate change. *Australian Journal of Earth Sciences*, *51*(3), 339–348. https://doi.org/10.1111/j.1400-0952.2004.01061.x

Gingele, F. X., De Deckker, P., & Hillenbrand, C.-D. (2001). Clay mineral distribution in surface sediments between Indonesia and NW Australia—Source and transport by ocean currents. *Marine Geology*, *179*(3–4), 135–146. https://doi.org/10.1016/S0025-3227(01)00194-3

Godfrey, J. S. (1996). The effect of the Indonesian throughflow on ocean circulation and heat exchange with the atmosphere: A review. *Journal of Geophysical Research*, *101*(C5), 12,217–12,237. https://doi.org/10.1029/95JC03860

Godfrey, J. S., & Mansbridge, J. V. (2000). Ekman transports, tidal mixing, and the control of temperature structure in Australia's northwest waters. *Journal of Geophysical Research*, *105*(C10), 24,021–24,044. https://doi.org/10.1029/2000JC900104

Gold, D. P., Burgess, P. M., & BouDagher-Fadel, M. K. (2017). Carbonate drowning successions of the Bird's Head, Indonesia. *Facies*, *63*(4), 87. https://doi.org/10.1007/s10347-017-0506-z

Gordon, A. L., & Kamenkovich, V. M. (2010). "Modeling and observing the Indonesian Throughflow" a special issue of dynamics of atmosphere and ocean. *Dynamics of Atmospheres and Oceans*, *50*(2), 113–114. https://doi.org/10.1016/j.dynatmoce.2010.04.003

Gordon, A. L., Sprintall, J., Van Aken, H. M., Susanto, D., Wijffels, S., Molcard, R., et al. (2010). The Indonesian throughflow during 2004–2006 as observed by the INSTANT program. *Dynamics of Atmospheres and Oceans*, *50*(2), 115–128. https://doi.org/10.1016/j.dynatmoce.2009.12.002

Gordon, A. L., Susanto, R. D., & Vranes, K. (2003). Cool Indonesian throughflow as a consequence of restricted surface layer flow. *Nature*, *425*(6960), 824–828. https://doi.org/10.1038/nature02038

Gourlan, A. T., Meynadier, L., & Allègre, C. J. (2008). Tectonically driven changes in the Indian Ocean circulation over the last 25 Ma: Neodymium isotope evidence. *Earth and Planetary Science Letters*, *267*(1-2), 353–364. https://doi.org/10.1016/j.epsl.2007.11.054

Gradstein, F., Ogg, J., Schmitz, M., & Ogg, G. (Eds.) (2012). *The geologic time scale 2012* (1st ed.). Boston: Elsevier.

Grelaud, M., Schimmelmann, A., & Beaufort, L. (2009). Coccolithophore response to climate and surface hydrography in Santa Barbara Basin, California, AD 1917–2004. *Biogeosciences*, *6*(10), 2025–2039. https://doi.org/10.5194/bg-6-2025-2009

Groeneveld, J., Henderiks, J., Renema, W., McHugh, C. M., De Vleeschouwer, D., Christensen, B. A., et al. (2017). Australian shelf sediments reveal shifts in Miocene Southern Hemisphere westerlies. *Science Advances*, *3*(5), 1–8. https://doi.org/10.1126/sciadv.1602567

Grunert, P., Soliman, A., Harzhauser, M., Müllegger, S., Piller, W. E., Roetzel, R., & Rögl, F. (2010). Upwelling conditions in the Early Miocene Central Paratethys Sea. *Geologica Carpathica*, *61*(2), 129–145. https://doi.org/10.2478/v10096-010-0006-3

Guerreiro, C., Cachão, M., & Nannoplankton, T. D. J. O. (2005). Calcareous nannoplankton as a tracer of the marine influence on the NW coast of Portugal over the last 14000 years. *Journal of Nannoplankton Research*, *27*(2), 159–172.

Hagino, K., & Okada, H. (2006). Intra- and infra-specific morphological variation in selected coccolithophore species in the equatorial and subequatorial Pacific Ocean. *Marine Micropaleontology*, *58*(3), 184–206. https://doi.org/10.1016/j.marmicro.2005.11.001, https://doi.org/10.1016/j.marmicro.2005.11.001

Hall, R. (2002). Cenozoic geological and plate tectonic evolution of SE Asia and the SW Pacific: Computer-based reconstructions, model and animations. *Journal of Asian Earth Sciences*, *20*(4), 353–431. https://doi.org/10.1016/S1367-9120(01)00069-4

Hall, R. (2012). Sundaland and Wallacea: Geology, plate tectonics and palaeogeography. In D. Gower, K. Johnson, J. Richardson, B. Rosen, L. Ruber, & S. Williams (Eds.), *Biotic evolution and environmental change in Southeast Asia* (pp. 32–78). Cambridge: Cambridge University Press. https://doi.org/10.1017/CBO9780511735882.005

Hall, R., Audley-Charles, M. G., Banner, F. T., Hidayat, S., & Tobing, S. L. (1988). Late Palaeogene–Quaternary geology of Halmahera, Eastern Indonesia: Initiation of a volcanic island arc. *Journal of the Geological Society*, *145*(4), 577–590. https://doi.org/10.1144/gsjgs.145.4.0577

Hall, R., Cottam, M. A., & Wilson, M. E. J. (2011). The SE Asian gateway: History and tectonics of the Australia–Asia collision. *Geological Society, London, Special Publications*, *355*(1), 1–6. https://doi.org/10.1144/SP355.1

Hammer, Ø., & Harper, D. A. T. (2006). *Paleontological data analysis* (1st ed.). Oxford: Blackwell Publishing Ltd.

Hammer, Ø., Harper, D. A. T., & Ryan, P. D. (2001). PAST—PAlaeontological STatistics (1st ed., pp. 1–31). Retrieved from www.toyen.uio.no, http://www.toyen.uio.no/~ohammer/past

Haq, B. U. (1980). Biogeographic history of Miocene calcareous nannoplankton and paleoceanography of the Atlantic Ocean. *Micropaleontology*, *26*(4), 414–443. https://doi.org/10.2307/1485353

Haq, B. U., & Lohmann, G. P. (1976). Early Cenozoic calcareous nannoplankton biogeography of the Atlantic Ocean. *Marine Micropaleontology*, *1*, 119–194. https://doi.org/10.1016/0377-8398(76)90008-6

Haug, G. H., & Tiedemann, R. (1998). Effect of the formation of the Isthmus of Panama on Atlantic Ocean thermohaline circulation. *Nature*, *393*(6686), 673–676. https://doi.org/10.1038/31447

He, Z., Feng, M., Wang, D., & Slawinski, D. (2015). Contribution of the Karimata Strait transport to the Indonesian Throughflow as seen from a data assimilation model. *Continental Shelf Research*, *92*, 16–22. https://doi.org/10.1016/j.csr.2014.10.007

Holbourn, A., Kuhnt, W., & Xu, J. (2011). Indonesian Throughflow variability during the last 140 ka: The Timor Sea outflow. *Geological Society, London, Special Publications*, *355*(1), 283–303. https://doi.org/10.1144/SP355.14

Imai, R., Sato, T., & Iryu, Y. (2017). Calcareous nannofossil assemblages of the upper Miocene to Pliocene Shimajiri Group on Okinawa-jima, Ryukyu Islands, southwestern Japan. *Journal of Asian Earth Sciences*, *135*, 16–24. https://doi.org/10.1016/j.jseaes.2016.12.011

Jatiningrum, R. S., & Sato, T. (2017). Sea-surface dynamics changes in the subpolar North Atlantic Ocean (IODP Site U1314) during late Pliocene climate transition based on calcareous nannofossil observation. *Open Journal of Geology*, *07*(10), 1538–1551. https://doi.org/10.4236/ojg.2017.710103

Jochum, M., Fox Kemper, B., Molnar, P. H., & Shields, C. (2009). Differences in the Indonesian seaway in a coupled climate model and their relevance to Pliocene climate and El Niño. *Paleoceanography*, *24*, PA1212. https://doi.org/10.1029/2008PA001678

Karas, C., Nürnberg, D., Bahr, A., Groeneveld, J., Herrle, J. O., Tiedemann, R., & deMenocal, P. B. (2017). Pliocene oceanic seaways and global climate. *Scientific Reports*, *7*(1), 39,842. https://doi.org/10.1038/srep39842

Karas, C., Nürnberg, D., Gupta, A. K., Tiedemann, R., Mohan, K., & Bickert, T. (2009). Mid-Pliocene climate change amplified by a switch in Indonesian subsurface throughflow. *Nature Geoscience*, *2*(6), 434–438. https://doi.org/10.1038/ngeo520

Karas, C., Nürnberg, D., Tiedemann, R., & Garbe Schönberg, D. (2011a). Pliocene climate change of the Southwest Pacific and the impact of ocean gateways. *Earth and Planetary Science Letters*, *301*(1–2), 117–124. https://doi.org/10.1016/j.epsl.2010.10.028

Karas, C., Nürnberg, D., Tiedemann, R., & Garbe Schönberg, D. (2011b). Pliocene Indonesian Throughflow and Leeuwin Current dynamics: Implications for Indian Ocean polar heat flux. *Paleoceanography*, *26*, PA2217. https://doi.org/10.1029/2010PA001949

Kinkel, H., Baumann, K. H., & Čepek, M. (2000). Coccolithophores in the equatorial Atlantic Ocean: Response to seasonal and Late Quaternary surface water variability. *Marine Micropaleontology*, *39*(1-4), 87–112. https://doi.org/10.1016/S0377-8398(00)00016-5

Knappertsbusch, M. (1993). Geographic distribution of living and Holocene coccolithophores in the Mediterranean Sea. *Marine Micropaleontology*, *21*(1-3), 219–247. https://doi.org/10.1016/0377-8398(93)90016-Q

Krebs, U., Park, W., & Schneider, B. (2011). Pliocene aridification of Australia caused by tectonically induced weakening of the Indonesian throughflow. *Palaeogeography, Palaeoclimatology, Palaeoecology*, *309*(1-2), 111–117. https://doi.org/10.1016/j.palaeo.2011.06.002

Kuhnt, W., Holbourn, A., Hall, R., Zuvela, M., & Käse, R. (2004). Neogene history of the Indonesian Throughflow. In P. Clift, W. Kuhnt, P. Wang, & D. Hayes (Eds.), *Continent-ocean interactions within East Asian marginal seas* (Vol. 149, pp. 299–320). Washington, DC: American Geophysical Union. https://doi.org/10.1029/149GM16

Kuhnt, W., Holbourn, A., Xu, J., Opdyke, B., De Deckker, P., Röhl, U., & Mudelsee, M. (2015). Southern Hemisphere control on Australian monsoon variability during the late deglaciation and Holocene. *Nature*, *6*(1), 5916. https://doi.org/10.1038/ncomms6916

Laskar, J., Robutel, P., Joutel, F., Gastineau, M., Correia, A. C. M., & Levrard, B. (2004). A long-term numerical solution for the insolation quantities of the Earth. *Astronomy & Astrophysics*, *428*(1), 261–285. https://doi.org/10.1051/0004-6361:20041335

Le Houedec, S., Meynadier, L., & Allègre, C. J. (2012). Nd isotope systematics on ODP Sites 756 and 762 sediments reveal major volcanic, oceanic and climatic changes in South Indian Ocean over the last 35Ma. *Earth and Planetary Science Letters*, *327-328*, 29–38. https://doi.org/10.1016/j.epsl.2012.01.019

Lees, J. A., Bown, P. R., & Mattioli, E. (2005). Problems with proxies? Cautionary tales of calcareous nannofossil paleoenvironmental indicators. *Micropaleontology*, *51*(4), 333–343. https://doi.org/10.2113/gsmicropal.51.4.333

Lisiecki, L. E., & Raymo, M. E. (2005). A Pliocene-Pleistocene stack of 57 globally distributed benthic δ^{18}O records. *Paleoceanography*, *20*, PA1003. https://doi.org/10.1029/2004PA001071

Lohmann, G. P., & Carlson, J. J. (1981). Oceanographic significance of Pacific Late Miocene calcareous nannoplankton. *Marine Micropaleontology*, *6*(5–6), 553–579. https://doi.org/10.1016/0377-8398(81)90021-9

Marino, M., & Flores, J.-A. (2002). Miocene to Pliocene calcareous nannofossil biostratigraphy at ODP Leg 177 Sites 1088 and 1090. *Marine Micropaleontology*, *45*(3–4), 291–307. https://doi.org/10.1016/S0377-8398(02)00033-6

Marino, M., Maiorano, P., Tarantino, F., Voelker, A., Capotondi, L., Girone, A., et al. (2014). Coccolithophores as proxy of seawater changes at orbital-to-millennial scale during middle Pleistocene Marine Isotope Stages 14–9 in North Atlantic core MD01-2446. *Paleoceanography*, *29*, 518–532. https://doi.org/10.1002/2013PA002574

Miller, K. G., Wright, J. D., Browning, J. V., Kulpecz, A., Kominz, M., Naish, T. R., et al. (2012). High tide of the warm Pliocene: Implications of global sea level for Antarctic deglaciation. *Geology*, *40*(5), 407–410. https://doi.org/10.1130/G32869.1

Molnar, P., & Cronin, T. W. (2015). Growth of the maritime continent and its possible contribution to recurring ice ages. *Paleoceanography*, *30*, 196–225. https://doi.org/10.1002/2014PA002752

Morse, J. W., & Berner, R. A. (1995). What determines sedimentary C/S ratios? *Geochimica et Cosmochimica Acta*, *59*(6), 1073–1077. https://doi.org/10.1016/0016-7037(95)00024-T

Okada, H., & Honjo, S. (1973). The distribution of oceanic coccolithophorids in the Pacific. *Deep-Sea Research and Oceanographic Abstracts*, *20*(4), 355–374. https://doi.org/10.1016/0011-7471(73)90059-4

Okada, H., & Wells, P. (1997). Late Quaternary nannofossil indicators of climate change in two deep-sea cores associated with the Leeuwin Current off Western Australia. *Palaeogeography, Palaeoclimatology, Palaeoecology*, *131*(3–4), 413–432. https://doi.org/10.1016/S0031-0182(97)00014-X

Patterson, M. O., McKay, R., Naish, T., Escutia, C., Jimenez-Espejo, F. J., Raymo, M. E., et al. (2014). Orbital forcing of the. *East Antarctic ice sheet during the Pliocene and Early Pleistocene*, *7*(11), 841–847. https://doi.org/10.1038/ngeo2273

Perch-Nielsen, K. (1985). Cenozoic calcareous nanofossils. In H. M. Bolli, J. B. Saunders, & K. Perch-Nielsen (Eds.), *Plankton stratigraphy volume 1* (Vol. 1, pp. 427–554). Cambridge: Cambridge University Press.

Philander, S. G., & Fedorov, A. V. (2003). Role of tropics in changing the response to Milankovich forcing some three million years ago. *Paleoceanography*, *18*(2), 1045. https://doi.org/10.1029/2002PA000837

Renaud, S., Ziveri, P., & Broerse, A. T. C. (2002). Geographical and seasonal differences in morphology and dynamics of the coccolithophore Calcidiscus leptoporus. *Marine Micropaleontology*, *46*(3-4), 363–385. https://doi.org/10.1016/S0377-8398(02)00081-6

Ridgway, K. R., & Godfrey, J. S. (2015). The source of the Leeuwin Current seasonality. *Journal of Geophysical Research: Oceans*, *120*, 6843–6864. https://doi.org/10.1002/2015JC011049

Riesselman, C. R., & Dunbar, R. B. (2013). Diatom evidence for the onset of Pliocene cooling from AND-1B, McMurdo Sound, Antarctica. *Palaeogeography, Palaeoclimatology, Palaeoecology*, *369*, 136–153. https://doi.org/10.1016/j.palaeo.2012.10.014

Rousseaux, C. S. G., Lowe, R., Feng, M., Waite, A. M., & Thompson, P. A. (2012). The role of the Leeuwin Current and mixed layer depth on the autumn phytoplankton bloom off Ningaloo Reef, Western Australia. *Continental Shelf Research*, *32*, 22–35. https://doi.org/10.1016/j.csr.2011.10.010

Saavedra-Pellitero, M., Baumann, K.-H., Flores, J.-A., & Gersonde, R. (2014). Biogeographic distribution of living coccolithophores in the Pacific sector of the Southern Ocean. *Marine Micropaleontology*, *109*, 1–20. https://doi.org/10.1016/j.marmicro.2014.03.003

Sageman, B. B., & Lyons, T. W. (2003). Geochemistry of fine-grained sediments and sedimentary rocks. In H. D. Holland & K. K. Turekian (Eds.), *Treatise on geochemistry* (pp. 115–158). Oxford: Pergamon. https://doi.org/10.1016/B0-08-043751-6/07157-7

Sagemann, J., Bale, S. J., Briggs, D. E. G., & Parkes, R. J. (1999). Controls on the formation of authigenic minerals in association with decaying organic matter: An experimental approach. *Geochimica et Cosmochimica Acta*, *63*(7–8), 1083–1095. https://doi.org/10.1016/S0016-7037(99)00087-3

Sarnthein, M., Grunert, P., Khélifi, N., Frank, M., & Nürnberg, D. (2017). Interhemispheric teleconnections: Late Pliocene change in Mediterranean outflow water linked to changes in Indonesian Through-Flow and Atlantic Meridional Overturning Circulation, a review and update. *International Journal of Earth Sciences*, *107*(2), 505–515. https://doi.org/10.1007/s00531-017-1505-6

Schiller, A., Wijffels, S. E., & Sprintall, J. (2007). Chapter 8 Variability of the Indonesian Throughflow: A Review and Model-to-Data Comparison. In H. Kawahata & Y. Awaya (Eds.), *Global Climate Change and Response of Carbon Cycle in the Equatorial Pacific and Indian Oceans and Adjacent Landmasses* (Vol. 73, pp. 175–494). Amsterdam, Netherlands: Elsevier. https://doi.org/10.1016/S0422-9894(06)73008-2

Schiller, A., Wijffels, S. E., Sprintall, J., Molcard, R., & Oke, P. R. (2010). Pathways of intraseasonal variability in the Indonesian Throughflow region. *Dynamics of Atmospheres and Oceans*, *50*(2), 174–200. https://doi.org/10.1016/j.dynatmoce.2010.02.003

Schott, F. A., Xie, S.-P., & McCreary, J. P. Jr. (2009). Indian Ocean circulation and climate variability. *Reviews of Geophysics*, *47*, RG1002. https://doi.org/10.1029/2007RG000245

Schrag, D. P., Adkins, J. F., McIntyre, K., Alexander, J. L., Hodell, D. A., Charles, C. D., & McManus, J. F. (2002). The oxygen isotopic composition of seawater during the Last Glacial Maximum. *Quaternary Science Reviews*, *21*(1-3), 331–342. https://doi.org/10.1016/S0277-3791(01)00110-X

Silva, A., Palma, S., & Moita, M. T. (2008). Coccolithophores in the upwelling waters of Portugal: Four years of weekly distribution in Lisbon bay. *Continental Shelf Research*, *28*(18), 2601–2613. https://doi.org/10.1016/j.csr.2008.07.009

Sniderman, J. M. K., Woodhead, J. D., Hellstrom, J., Jordan, G. J., Drysdale, R. N., Tyler, J. J., & Porch, N. (2016). Pliocene reversal of late Neogene aridification. *Proceedings of the National Academy of Sciences of the United States of America*, *113*(8), 1999–2004. https://doi.org/10.1073/pnas.1520188113

Sokal, R. R., & Rohlf, F. J. (1995). *Biometry* (3rd ed.). New York: W. H. Freeman and Company.

Spooner, M. I., De Deckker, P., Barrows, T. T., & Fifield, L. K. (2011). The behaviour of the Leeuwin Current offshore NW Australia during the last five glacial–interglacial cycles. *Global and Planetary Change*, *75*(3–4), 119–132. https://doi.org/10.1016/j.gloplacha.2010.10.015

Stax, R., & Stein, R. (1995). Data report: Organic carbon and carbonate records from Detroit seamount and Patton-Murray Seamount: Results from sites 882 and 887 (North Pacific Transect). *Proceedings of the Ocean Drilling Program, Scientific Results*, *145*, 645–655.

Susanto, R. D., & Song, Y. T. (2015). Indonesian throughflow proxy from satellite altimeters and gravimeters. *Journal of Geophysical Research: Oceans*, *120*, 2844–2855. https://doi.org/10.1002/2014JC010382

Takahashi, K., & Okada, H. (2000). The paleoceanography for the last 30,000 years in the southeastern Indian Ocean by means of calcareous nannofossils. *Marine Micropaleontology*, *40*(1-2), 83–103. https://doi.org/10.1016/S0377-8398(00)00033-5

Tate, G. W., McQuarrie, N., Tiranda, H., van Hinsbergen, D. J. J., Harris, R., Zachariasse, W. J., et al. (2017). Reconciling regional continuity with local variability in structure, uplift and exhumation of the Timor orogen. *Gondwana Research*, *49*, 364–386. https://doi.org/10.1016/j.gr.2017.06.008

Thompson, P. A., Wild-Allen, K., Lourey, M., Rousseaux, C., Waite, A. M., Feng, M., & Beckley, L. E. (2011). Nutrients in an oligotrophic boundary current: Evidence of a new role for the Leeuwin Current. *Progress in Oceanography*, *91*(4), 345–359. https://doi.org/10.1016/j.pocean.2011.02.011

Thunell, R., Tappa, E., Pride, C., & Kincaid, E. (1999). Sea-surface temperature anomalies associated with the 1997–1998 El Niño recorded in the oxygen isotope composition of planktonic foraminifera. *Geology*, *27*(9), 843–846. https://doi.org/10.1130/0091-7613(1999)027<0843:SSTAAW>2.3.CO;2

Wade, B. S., & Bown, P. R. (2006). Calcareous nannofossils in extreme environments: The Messinian salinity crisis, Polemi Basin, Cyprus. *Palaeogeography, Palaeoclimatology, Palaeoecology*, *233*(3–4), 271–286. https://doi.org/10.1016/j.palaeo.2005.10.007

Waelbroeck, C., Labeyrie, L., Michel, E., Duplessy, J. C., McManus, J. F., Lambeck, K., et al. (2002). Sea-level and deep water temperature changes derived from benthic foraminifera isotopic records. *Quaternary Science Reviews*, *21*(1-3), 295–305. https://doi.org/10.1016/S0277-3791(01)00101-9

Waite, A. M., Thompson, P. A., Pesant, S., Feng, M., Beckley, L. E., Domingues, C. M., et al. (2007). The Leeuwin Current and its eddies: An introductory overview. *Deep-Sea Research Part II: Topical Studies in Oceanography*, *54*(8-10), 789–796. https://doi.org/10.1016/j.dsr2.2006.12.008

Wara, M. W., Ravelo, A. C., & Delaney, M. L. (2005). Permanent El Niño-like conditions during the Pliocene warm period. *Science*, *309*(5735), 758–761. https://doi.org/10.1126/science.1112596

Ward, J. H. Jr. (1963). Hierarchical grouping to optimize an objective function. *Journal of the American Statistical Association*, *58*(301), 236–244. https://doi.org/10.1080/01621459.1963.10500845

Wei, G., Li, X.-H., Liu, Y., Shao, L., & Liang, X. (2006). Geochemical record of chemical weathering and monsoon climate change since the early Miocene in the South China Sea. *Paleoceanography*, *21*, PA4214. https://doi.org/10.1029/2006PA001300

Wijeratne, S., Pattiaratchi, C., & Proctor, R. (2018). Estimates of surface and subsurface boundary current transport around Australia. *Journal of Geophysical Research: Oceans*, *123*, 3444–3466. https://doi.org/10.1029/2017JC013221

Wilson, B. (2013). *The biogeography of the Australian North West Shelf: Environmental change and life's response*. San Diego, CA: Elsevier.

Xu, J., Holbourn, A., Kuhnt, W., Jian, Z., & Kawamura, H. (2008). Changes in the thermocline structure of the Indonesian outflow during Terminations I and II. *Earth and Planetary Science Letters*, *273*(1-2), 152–162. https://doi.org/10.1016/j.epsl.2008.06.029

Xu, J., Kuhnt, W., Holbourn, A., Andersen, N., & Bartoli, G. (2006). Changes in the vertical profile of the Indonesian Throughflow during termination II: Evidence from the Timor Sea. *Paleoceanography*, *21*, PA4202. https://doi.org/10.1029/2006PA001278

Young, J. R. (1998). Neogene. In P. R. Bown (Ed.), *Calcareous nannofossil biostratigraphy*, (1st ed.pp. 225–265). Cambridge: Chapman & Hall. https://doi.org/10.1007/978-94-011-4902-0_8

Young, J. R., Bown, P. R., & Lees, J. A. (Eds.) (2014). Nannotax 3. Retrieved from http://www.mikrotax.org/Nannotax3/

Young, J. R., Pratiwi, S., Su, X., & Expedition 359 Scientists (2017). Data report: surface seawater plankton sampling for coccolithophores undertaken during IODP Expedition 359. In C. Betzler, G. P. Eberli, C. A. Alvarez-Zarikian, & Expedition 359 Scientists (Eds.), *Proceedings of the International Ocean Discovery Program* (Vol. 359, pp. 1–7). College Station, TX. https://doi.org/10.14379/iodp.proc.359.111.2017

Zhang, Z., Lowe, R., Ivey, G., Xu, J., & Falter, J. (2016). The combined effect of transient wind-driven upwelling and eddies on vertical nutrient fluxes and phytoplankton dynamics along Ningaloo Reef, Western Australia. *Journal of Geophysical Research: Oceans*, *121*, 4994–5016. https://doi.org/10.1002/2016JC011791

Ziveri, P., Baumann, K.-H., Böckel, B., Bollmann, J., & Young, J. R. (2004). Biogeography of selected Holocene coccoliths in the Atlantic Ocean. In *Coccolithophores* (pp. 403–428). Berlin, Heidelberg: Springer. https://doi.org/10.1007/978-3-662-06278-4_15

Zou, J., Shi, X., Liu, Y., Liu, J., Selvaraj, K., & Kao, S.-J. (2012). Reconstruction of environmental changes using a multi-proxy approach in the Ulleung Basin (Sea of Japan) over the last 48 ka. *Journal of Quaternary Science*, *27*(9), 891–900. https://doi.org/10.1002/jqs.2578

Zuraida, R., Holbourn, A., Nürnberg, D., Kuhnt, W., Dürkop, A., & Erichsen, A. (2009). Evidence for Indonesian Throughflow slowdown during Heinrich events 3-5. *Paleoceanography*, *24*, PA2205. https://doi.org/10.1029/2008PA001653